Quaternary Science Reviews 284 (2022) 107467

Contents lists available at ScienceDirect

Quaternary Science Reviews

journal homepage: www.elsevier.com/locate/quascirev

Reconstructing Late Quaternary precipitation and its source on the southern Cape coast of South Africa: A multi-proxy paleoenvironmental record from Vankervelsvlei

P. Strobel [a, *], M. Bliedtner [a], A.S. Carr [b], J. Struck [a], N. du Plessis [c, d], B. Glaser [e], M.E. Meadows [c, f, g], L.J. Quick [d], M. Zech [h], R. Zech [a], T. Haberzettl [i]

[a] Physical Geography, Institute of Geography, Friedrich Schiller University Jena, Jena, Germany
[b] School of Geography, Geology and the Environment, University of Leicester, Leicester, UK
[c] Department of Environmental and Geographical Science, University of Cape Town, Rondebosch, South Africa
[d] African Centre for Coastal Palaeoscience, Nelson Mandela University, Port Elizabeth, South Africa
[e] Institute of Agricultural and Nutritional Sciences, Soil Biogeochemistry, Martin-Luther University Halle-Wittenberg, Halle (Saale), Germany
[f] School of Geographic and Ocean Sciences, Nanjing University, Nanjing, China
[g] College of Geography and Environmental Sciences, Jiajiang Normal University, Jinhua, China
[h] Heisenberg Chair of Physical Geography with Focus on Paleoenvironmental Research, Institute of Geography, Technische Universität Dresden, Dresden, Germany
[i] Physical Geography, Institute for Geography and Geology, University of Greifswald, Greifswald, Germany

ARTICLE INFO

Article history:
Received 16 December 2021
Received in revised form
15 March 2022
Accepted 20 March 2022
Available online 6 April 2022

Handling Editor: Yan Zhao

Keywords:
Paleoclimate
Leaf waxes
Hemicellulose sugars
Compound-specific oxygen
Hydrogen and carbon isotopes
Relative humidity
Coupled $\delta^2H_{n\text{-alkane}}$–$\delta^{18}O_{sugar}$ paleohygrometer

ABSTRACT

The Late Quaternary climate history of South Africa and, in particular, potential changes in atmospheric circulation have been subject to considerable debate. To some extent, this is due to a scarcity of natural archives, and on the other hand the available indirect hydrological proxies are not suited to distinguishing between precipitation originating from temperate Westerlies and tropical Easterlies. This study presents a paleoenvironmental record from Vankervelsvlei, a wetland located on the southern Cape coast in the year-round rainfall zone of South Africa. A 15 m long sediment record was retrieved from this site and analysed using a multi-proxy approach. This includes, for the first time in this region, analysis of both compound-specific δ^2H and $\delta^{18}O$ from leaf wax-derived *n*-alkanes and hemicellulose-derived sugars, respectively, to investigate hydrological changes during the Late Quaternary. Our data suggest the driest conditions of the past ~250 ka likely occurred from MIS 6 to MIS 5e, which still caused sediment deposition at Vankervelsvlei, and MIS 2, during which time there was an absence of sedimentation. Moist conditions occurred from MIS 5e to 5a and during parts of MIS 3, while drier conditions prevailed between MIS 5a and early MIS 3 and at the transition from MIS 3 to MIS 2. Besides changes in the amount and proportional contribution of precipitation contributions from Westerlies during glacial and Easterlies during interglacial periods, relative sea-level change affected the continentality of Vankervelsvlei, with a distinct impact on the sites hydrological balance. High-resolution analyses of the Middle- and Late-Holocene parts of the record show moist conditions and increased Easterly/locally-derived summer precipitation contributions from 7230 $^{+160}/_{-210}$ to 4890 $^{+280}/_{-180}$ cal BP and after 2840 $^{+350}/_{-330}$ cal BP. Dry conditions, accompanied by the reduction of Easterly/locally-derived summer rainfall and increased seasonality occurred from 4890 $^{+280}/_{-180}$ to 2840 $^{+350}/_{-330}$ cal BP. Our findings highlight that source and seasonality of precipitation play a major role in the hydrological balance of the southern Cape coastal region. By comparing the Vankervelsvlei record to other regional studies, we infer a coherent trend in the overall moisture evolution along South Africa's southern Cape coast during the Late Quaternary.

1. Introduction

South Africa is a key region for paleoenvironmental

* Corresponding author. Physical Geography, Institute of Geography, Friedrich Schiller University Jena, Loebdergraben 32, 07743, Jena, Germany.
E-mail address: paul.strobel@uni-jena.de (P. Strobel).

https://doi.org/10.1016/j.quascirev.2022.107467

reconstructions, because of its location between the temperate and the tropical atmospheric circulation systems, i.e. the temperate Westerlies and the monsoon-driven Easterlies (Chase and Meadows, 2007; Cockcroft et al., 1987; Haberzettl et al., 2014; van Zinderen Bakker, 1976). However, there is a general paucity of Late Quaternary terrestrial paleoenvironmental records, largely due to South Africa's essentially erosive Cenozoic landscape history, which has limited the potential for the accumulation of terrestrial sedimentary deposits (Haberzettl et al., 2014; Quick et al., 2015; van Zinderen Bakker, 1976; Wündsch et al., 2018). Despite this scarcity of terrestrial archives in South Africa, several proxy and model-based paleoenvironmental studies have been carried out during the past decades. Most of those studies use rather discontinuous sediment records, leading to a contrasting interpretations of South Africa's hydrological evolution during the Late Quaternary; interpretations further complicated by the use of various indirect paleohydrological proxies (e.g. Chase and Meadows, 2007; Chase and Quick, 2018; Cockcroft et al., 1987; Reinwarth et al., 2013; Singarayer and Burrough, 2015; Wündsch et al., 2016; Zhao et al., 2016).

To provide clearer insights into paleohydrological change, it has been proposed that compound-specific stable isotope analyses of leaf wax-derived long-chain *n*-alkanes (>C_{25}) are a proxy with great potential to complement established methodological approaches in sediment archives (e.g. Hahn et al., 2017; Hahn et al., 2021; Miller et al., 2020; Strobel et al., 2021; Strobel et al., 2019). Long-chain *n*-alkanes are produced as leaf waxes in higher terrestrial plants and remain well preserved in soils and sediments over millennia due to their low water solubility and high resistance against degradation (Eglinton and Eglinton, 2008; Sachse et al., 2012; Sessions, 2016). They serve as valuable biomarkers because their hydrogen isotope composition ($\delta^2H_{n\text{-alkane}}$) is driven by the isotopic composition of precipitation (δ^2H_p) (Herrmann et al., 2017; Strobel et al., 2020; Struck et al., 2020). However, various fractionation processes occur from the moisture source to its fixation in the leaf waxes, which may bias the precipitation isotope signal and complicate interpretations, with evapotranspirative enrichment being a prominent factor (Sachse et al., 2012; Sessions, 2016; Zech et al., 2015). In the mid-latitudes, the $\delta^2H_{n\text{-alkane}}$ signal is mainly controlled by the isotopic signal of the moisture source (Schäfer et al., 2018; Strobel et al., 2020; Wirth and Sessions, 2016). However, in existing studies using $\delta^2H_{n\text{-alkane}}$ in a single water-isotope-approach for paleohydrological reconstruction it is challenging to disentangle precipitation source and amount, and especially the influence of evapotranspirative enrichment (e.g. Hahn et al., 2017; Miller et al., 2020; Strobel et al., 2019). Similarly, single isotope studies using stable oxygen isotopes ($\delta^{18}O$) from speleothems in this region, have also found it challenging to disentangle the effects of temperature and precipitation source (Bar-Matthews et al., 2010; Braun et al., 2019, 2020; Talma and Vogel, 1992). $\delta^{18}O_{cellulose}$ (Heyng et al., 2014; Shi et al., 2019a, 2019b; Sternberg and DeNiro, 1983; Wissel et al., 2008) and $\delta^{18}O$ of hemicellulose-derived sugar biomarkers ($\delta^{18}O_{sugar}$) (Struck et al., 2020; Tuthorn et al., 2014; Zech and Glaser, 2009; Zech et al., 2012, 2014) may also be used for paleoclimatic and -hydrological research. Similar to leaf waxes, hemicellulose-derived sugars record the isotopic composition of precipitation ($\delta^{18}O_p$) and are also modulated by evaporative enrichment, further highlighting the challenges of single-water isotope studies.

For organic-rich sediments there is potential to disentangle some of these effects by measuring more than one water isotope from the same sample. It has been suggested that by coupling $\delta^2H_{n\text{-alkane}}$ and $\delta^{18}O_{sugar}$ analyses, it is possible to disentangle changes in δ^2H_p and $\delta^{18}O_p$ and changes in evapotranspirative leaf and lake water enrichment. For instance, Voelker et al. (2014) used δ^2H and $\delta^{18}O$ of tree-ring cellulose to reconstruct relative air humidity. Another approach to reconstruct air humidity by coupling $\delta^2H_{n\text{-alkane}}$ and $\delta^{18}O_{sugar}$ results ('paleohygrometer'). This has been validated in climate chamber experiments (Hepp et al., 2021) as well as for topsoils in Europe (Hepp et al., 2020), South America (Tuthorn et al., 2015), Ethiopia (Lemma et al., 2021) and South Africa (Strobel et al., 2020). Both approaches have already been applied successfully for paleoclimate reconstructions, for example in loess–paleosol sequences (Hepp et al., 2017; Zech et al., 2013), on subfossil wood (Voelker et al., 2015) and in lacustrine sediments (Hepp et al., 2015, 2019).

Given the demonstrated complexities of reconstructing paleoclimate and -hydrology on the southern Cape coast, the potential advantages of this coupled isotope approach are readily apparent. Here we applied this coupled approach to a sediment record from Vankervelsvlei, a fen located at South Africa's southern Cape coast spanning large parts of the Late Quaternary (Irving, 1998; Irving and Meadows, 1997; Quick et al., 2016). In contrast to other near coastal wetlands in the Wilderness region, Vankervelsvlei has not been influenced by sea water intrusions in the past. Our study aims to support, refine and expand the previously published study by Strobel et al. (2019), who investigated parts of the composite record presented here, at a higher temporal-resolution, with new proxies and with an updated and extended chronology. Using this combined multi-isotope approach, incorporating both water isotopes, i.e. compound-specific $\delta^2H_{n\text{-alkane}}$ and $\delta^{18}O_{sugar}$, as well as compound-specific $\delta^{13}C_{n\text{-alkane}}$, together with established assemblages of inorganic and organic elemental proxies, this paper aims to:

i) infer past variations in precipitation source and moisture availability at Vankervelsvlei, and to consider the potential regional paleoclimatic scenarios that may have driven such variability and
ii) provide a high-resolution terrestrial record for the Middle- and Late-Holocene to disentangle changes in local precipitation source, moisture availability and relative humidity by coupling of $\delta^2H_{n\text{-alkane}}$ and $\delta^{18}O_{sugar}$.

2. Site description

Vankervelsvlei is situated at 152 m above present sea level (a.s.l.), about 5 km inland from the Indian Ocean coast on South Africa's southern Cape (Fig. 1). Vankervelsvlei is an irregular shaped depression enclosed by cemented coastal dunes, which are approximately 250 to 205 ka old (Bateman et al., 2011; Illenberger, 1996), that separate Vankervelsvlei from the present coast (Fig. 1D). These Middle to Late Pleistocene dune systems and landwards even older coversand deposits are unconformably underlain by Quartzites of the Table Mountain Group (Cape Supergroup) and Palaeozoic (Ordovician-Silurian) Peninsula Formation sandstones (Carr et al., 2010; Johnson et al., 2006). Shallow and nutrient-poor generally acidic and leached soils predominate the region (e.g., Alisols and Luvisols) (Geldenhuys, 1988; Irving and Meadows, 1997). The potential natural vegetation consists of variations of Fynbos and Afromontane forest (Mucina and Rutherford, 2006). Today, the steep slopes of the catchment are used as a commercial pine (*Pinus*) plantation and the vegetation growing on the fen predominantly consists of Cyperaceae with some ferns (Pteridophytes) and mosses (Bryophytes) (Quick et al., 2016). The fen itself has an area of 0.34 km^2 and the catchment comprises an area of 4.1 km^2 (Fig. 1D). The morphology of the catchment ranges from 330 to 152 m a.s.l. (Database: SRTM 1 arc-second (NASA, 2013)) with no permanent surface inflow and no surface outlet (Fig. 1D).

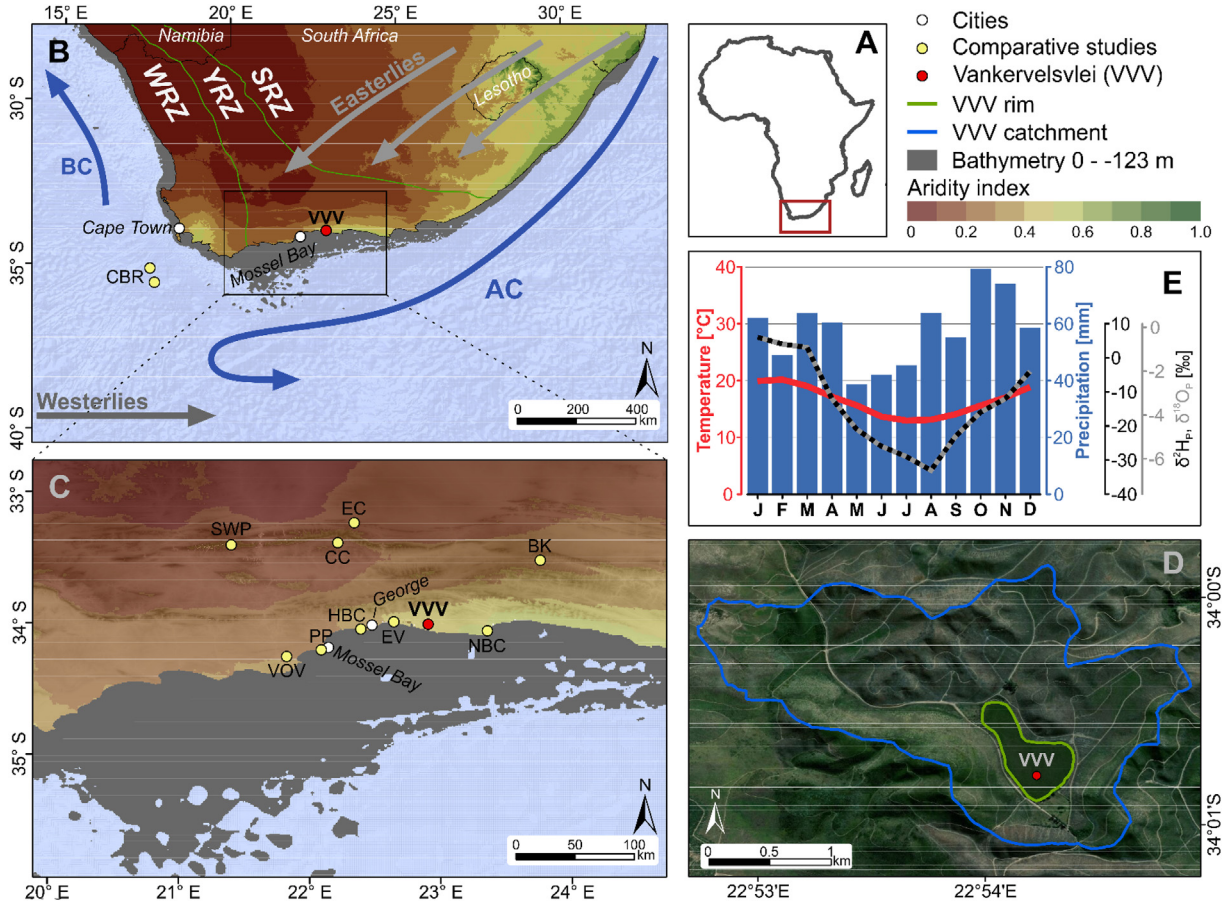

Fig. 1. A) Simplified map of Africa. The red box is magnified in B). **B**) Location of Vankervelsvlei (red dot, labelled VVV) and the three major rainfall zones of South Africa, i.e. winter-rainfall zone (WRZ), year-round rainfall zone (YRZ) and summer rainfall zone (SRZ) after *Chase and Meadows (2007)* derived from Worldclim 2 dataset (*Fick and Hijmans, 2017*). Additionally, the circumpolar Westerlies, the tropical Easterlies, the Agulhas Current (AC), the Benguela Current (BC) and the Aridity Index (brown to green colour, *Trabucco and Zomer, 2019*) are depicted. The grey area shows the part of the shelf that was exposed during the sea level low stand of −123 m (British Oceanographic data centre, 2014; *Waelbroeck* et al., *2002*). The yellow dots show the location of the Cape Basin Record (*CBR; Peeters et al., 2004*). **C**) Vankervelsvlei and selected studies mentioned in the text (yellow dots: Voëlvlei (*VOV, Strobel et al., 2020*) Pinnacle Point (*PP, Bar-Matthews et al., 2010*; *Braun* et al., *2019*), Herolds Bay Cave (*HBC, Braun et al., 2020*), Eilandvlei (*EV, Quick et al., 2018*; *Wündsch* et al., *2018*), Nelson Bay Cave (*NBC, Cohen and Tyson, 1995*), Baviaanskloof (*BK, Chase et al., 2020*), Efflux Cave (*EC, Braun et al.,2020*), Cango Cave (*CC, Talma and Vogel, 1992*), Seweweekspoort (*SWP, Chase et al., 2017*)). **D**) Topographic map (ESRI Inc., 2020) including catchment and rim of Vankervelsvlei as well as the coring position. **E**) Climate diagram illustrating the seasonal variability of precipitation and temperature (1981–2020; Station: George Airport (*DWD Climate Data Center, 2020*)) as well as the variability of δ^2H_p and $\delta^{18}O_p$ (*Bowen, 2020*; *Bowen and Revenaugh, 2003*) at Vankervelsvlei. (For interpretation of the references to colour in this figure legend, the reader is referred to the Web version of this article.)

The past and present climate of southern Africa is driven by variable interactions of oceanic (the Benguela current on the west coast and the Agulhas current along the east and south coasts) and atmospheric circulation systems (Tyson and Preston-Whyte, 2000) (Fig. 1 B). Today, three major rainfall seasonality zones occur in South Africa. In the eastern and central parts of the country, the majority of the rainfall is associated with tropical moisture-bearing atmospheric circulation systems (Easterlies) during the austral summer (summer rainfall zone, SRZ). A narrow belt along the west coast is dominated by precipitation supplied by temperate Westerlies during the austral winter (winter rainfall zone, WRZ) (Fig. 1 B). The year-round rainfall zone (YRZ) represents the intermediate area between the SRZ and WRZ and receives rainfall from both systems throughout the year (Fig. 1 B) (Engelbrecht et al., 2015; Scott and Lee-Thorp, 2004), which includes the relatively humid southern Cape coast where Vankervelsvlei is located.

Besides the Atlantic and Indian Ocean as major sources of precipitation (Westerlies (austral winter) and Easterlies (austral summer)), on the southern Cape coast, ridging anticyclones produce onshore flow that leads to orographic rainfall from local sources that can occur year-round (Engelbrecht and Landman, 2016; Weldon and Reason, 2014). Analysis of recent precipitation data from George Airport, located ca. 50 km west of Vankervelsvlei (Fig. 1C), reveals a mean annual precipitation of 690 mm·a^{-1} for the coastal areas of the YRZ, but highly variable precipitation during recent years, without significant seasonality (ranging from 375 to 1220 mm·a^{-1}; 1981–2020) (DWD Climate Data Center, 2020) (Fig. 1C, E).

Although the annual precipitation distribution is quite uniform, δ^2H_p and $\delta^{18}O_p$ are highly variable throughout the year (Braun et al., 2017; Harris et al., 2010). The modelled isotopic composition of precipitation (δ^2H_p, $\delta^{18}O_p$) is ^{2}H- and ^{18}O-depleted during winter (−26 to −33‰ and −5.5 to −6.5‰ for δ^2H_p and $\delta^{18}O_p$, respectively), and ^{2}H- and ^{18}O-enriched during summer periods (−4 to +6‰ and −2.0 to −0.8 for δ^2H_p and $\delta^{18}O_p$, respectively) (Table 1) (Bowen, 2020; Bowen et al., 2005), which is in good agreement with recently observed data (Braun et al., 2017; Harris et al., 2010). Precipitation of local origin is isotopically ^{2}H- and ^{18}O-enriched (Braun et al., 2017). Temperatures are generally uniform with an annual mean of 16.5 °C (1989–2020) (DWD Climate Data Center, 2020). South-westerly winds predominate in the region and mountain wind conditions, especially in the winter months, can

periodically result in anomalously high temperatures in the area (Quick et al., 2016).

3. Material and methods

3.1. Composite sediment record compilation

For this study, three parallel piston cores (UWITEC, Mondsee, Austria) (VVV16-1, 0.8–13.0 m depth including core loss between 2 and 3.9 m depth; VVV16-2, 9.8–13.8 m depth, VVV16-6; 4–15.0 m depth; inner diameter 90 mm) were retrieved from Vankervelsvlei (34.013 °S; 22.904 °E) (Fig. 1 C). The topmost sediments were recovered using a self-made push core device (VVV16-4; 0–0.8 m depth; inner diameter 90 mm). Together these four drives equated to a composite sediment core depth of 15 m with a gap from 3.9 to 2 m composite depth due to core loss.

3.2. Chronology

3.2.1. Radiocarbon dating

^{14}C ages were determined on seven organic plant-macro particles and nine bulk TOC samples at the Poznan Radiocarbon Laboratory, Poland. Besides three ages at the top of the sequence, which were recently published by du Plessis et al. (2021), ^{14}C ages of organic macro particles and bulk TOC were published by Strobel et al. (2019) (see Supplementary Information; Table S1).

3.2.2. Optically stimulated luminescence dating (OSL)

Nine samples were obtained for OSL dating. Short sections of the core tubes (~20 cm) were opened under subdued red light at the University of Leicester and from these ~5 cm subsamples were obtained. The chronology is largely based on the analysis of coarse grained quartz, except for the lowermost two samples where the K-feldspar fraction was used for age determination (see Supplementary Information for more details on the OSL dating methods).

3.2.3. Age-depth modelling

For age-depth modelling in the lower part of the record (15.0–11.18 m composite depth) only the obtained OSL ages were used. For the upper part of the sediment sequence, ^{14}C ages on organic plant-macro particles and bulk organic matter published by Strobel et al. (2019) and du Plessis et al. (2021) were recalibrated with the SHCal20 calibration curve (Hogg et al., 2020). All calibrations were done with the online version of the Calib 8.2 software (Stuiver et al., 2020). The final age-depth profile relation was modelled with the R software package Bacon 2.4.3 (Blaauw and Christen, 2011), using the same calibration data set. In the following, ages are reported as median ages including the upper and lower limit of the 95% confidence interval.

3.3. Physical properties and elemental analyses

Sample aliquots were freeze-dried (−50 °C, <72 h), and aluminium (Al) and iron (Fe) contents were measured with an ICP-OES 725-ES (VARIAN, California, USA) at Friedrich Schiller University Jena. 0.2 g of the samples were processed using a microwave-assisted modified aqua regia digestion of 2 ml HCl (32%) and 4 ml HNO_3 (65%). Error estimates are based on triple measurements of five individual samples (relative errors: Al <5.6%; Fe: <5.1%). Samples of the reference material LGC6 187 (river sediment) were measured as well to calculate the relative analytical error which was <0.79% and <0.49% for Al and Fe, respectively.

X-ray fluorescence (XRF) data were obtained using an ITRAX XRF-core scanner (Croudace et al., 2006) at GEOPOLAR (University of Bremen). Scanning was done with a Mo-tube with a step size of 1 cm and a count time of 30 s per step; tube settings were kept constant for all cores using a voltage of 30 kV and a current of 30 mA. Element intensities were given as counts (cts), which were subsequently normalised by the total number of counts to minimize a bias resulting from matrix changes and tube aging.

3.4. Leaf wax analyses

Total lipids of the sediment samples (0.3–38.3 g) were extracted with 40 ml dichloromethane (DCM) and methanol (MeOH) (9/1, v/v) using an ultrasonic bath over three 15 min cycles at Friedrich Schiller University Jena. The total lipid extract was separated by solid phase extraction using aminopropyl silica gel (Supelco, 45 μm) as stationary phase. The *n*-alkanes were eluted with 4 ml hexane and further purified over coupled silvernitrate ($AgNO_3$–; Supelco, 60–200 mesh) - zeolite (Geokleen) pipette columns. The *n*-alkanes trapped in the zeolite were subsequently dissolved in hydrofluoric acid and recovered by liquid-liquid extraction using *n*-hexane. An Agilent 7890 gas chromatograph equipped with an Agilent HP5MS column (30 m, 320 μm, 0.25 μm film thickness) and a flame ionization detector (GC-FID) was used for identification and quantification of the *n*-alkanes, relative to external *n*-alkane standards (*n*-alkane mix *n*-C_{21} - *n*-C_{40}, Supelco).

Compound-specific stable hydrogen isotope analyses of the C_{29} and C_{31} *n*-alkanes were carried out on an IsoPrime vision IRMS, coupled to an Agilent 7890A GC via a GC5 pyrolysis or combustion interface operating in pyrolysis modus with a MaxChrome and silver wool packed reactor at 1050 °C. Samples were injected splitless with a split–splitless injector. The GC was equipped with a 30 m fused silica column (HP5-MS, 0.32 mm, 0.25 μm). Each sample was analysed in triplicate, except 13 samples in the lower part of the sequence due to insufficient compound abundance. $\delta^2H_{n\text{-alkane}}$ was measured against calibrated H_2 reference gas and all values are reported in per mille against VSMOW. The precision was checked by co-analysing a standard alkane mixture (*n*-C_{27}, *n*-C_{29}, *n*-C_{33}) with known isotope composition (Arndt Schimmelmann, University of Indiana), injected in duplicate every nine runs. All measurements were corrected for drift and amount dependency, relative to the standard values in each sequence. Triplicates for the C_{29} and C_{31} alkanes in the upper part and lower part of the sequence had a standard deviation of <3.7‰ and <8.0‰, respectively, except for two samples in the upper part (VVV16_618 and VVV16_648 with 11‰ and 16‰, respectively). The analytical error for the standards was <1.5 and < 3.2‰ for the upper and lower part of the sequence (n = 44 and 40). The H_3^+ factor was checked every two days and stayed stable at 3.9 ± 0.1 during measurements. An amount weighted mean of the δ^2H signals from the C_{29} and C_{31} *n*-alkanes

Table 1
Modelled hydrogen and oxygen isotopic composition of the contemporary precipitation at Vankervelsvlei (Lat: 34.013° S; Lon: 22.904° E; Elevation: 152 m) (Bowen, 2020; Bowen et al., 2005).

	Jan	Feb	Mar	Apr	May	Jun	Jul	Aug	Sep	Oct	Nov	Dec
δ^2H_p [‰ vs. V-SMOW]	6	4	3	−12	−21	−26	−29	−33	−23	−16	−12	−4
$\delta^{18}O_p$ [‰ vs. V-SMOW]	−0.8	−0.8	−1.6	−3.7	−4.8	−5.5	−5.7	−6.5	−4.9	−3.9	−3.3	−2.0

was calculated and is referred to as $\delta^2H_{n\text{-alkane}}$ in the following.

Compound-specific stable carbon isotope analyses of C_{29} and C_{31} *n*-alkanes were carried out on an IsoPrime vision IRMS, coupled to an Agilent 7890A GC via a GC5 pyrolysis or combustion interface operating in combustion modus with a CuO packed reactor at 850 °C. Samples were injected splitless with a split–splitless injector. The GC was equipped with 30 m fused silica column (HP5-MS, 0.32 mm, 0.25 μm). $\delta^{13}C$ values were calibrated against CO_2 reference gas of known isotopic composition and all carbon isotope values are given in per mille against VPDB. Triplicate injections were conducted for each sample and measurement accuracy was controlled in the same way as for the δ^2H analyses. Triplicates for the C_{29} and C_{31} alkanes had a standard deviation of <0.3‰, the analytical error for the standards was <0.2‰ ($n = 38$). An amount weighted mean of the $\delta^{13}C$ signals from the C_{29} and C_{31} *n*-alkanes was calculated and is referred to as $\delta^{13}C_{n\text{-alkane}}$ in the following.

3.5. Sugar biomarker analyses

Hemicellulose-derived sugars were hydrolytically extracted from 28 dried samples (0.1–1.9 g, depending on TOC content) at the Institute of Agricultural and Nutritional Sciences, Soil Biogeochemistry, Martin Luther University Halle-Wittenberg. Samples were extracted with 10 ml of 4 M trifluoroacetic acid at 105 °C for 4 h, as described in Amelung et al. (1996). Thereafter, samples were vacuum-filtered over glass fibre filters and the extracted sugars were cleaned according to Zech and Glaser (2009) using XAD-7 and Dowex 50WX8 columns to remove humic-like substances and cations. The purified sugar samples were rotary evaporated and derivatised with methylboronic acid (4 mg in 400 μl pyridine) at 60 °C for 1 h. 5α-Androstane and 3-O-Methyl-Glucose were used as internal standards.

The compound-specific oxygen isotope measurements were performed on a Trace GC 2000 coupled to a Delta V Advantage IRMS using an ^{18}O-pyrolysis reactor (GC IsoLink) and a ConFlo IV interface (all devices from Thermo Fisher Scientific, Bremen, Germany). Samples were injected in splitless mode and measured in triplicates. For measurement precision, standard blocks of derivatised sugars (arabinose, fucose, xylose) at various concentrations and known $\delta^{18}O$ values were measured. Arabinose and Fucose were less abundant compared to Xylose and therefore not considered for compound-specific oxygen isotope analyses. All measurements were corrected for drift and amount dependency, as well as for hydrolytically introduced oxygen atoms which form carbonyl groups within the sugar molecules (Zech and Glaser, 2009). The standard deviation of the sugar sample triplicate measurements for the upper and lower part of the sequence were <2.0‰ and <3.1‰, respectively. Standard duplicate measurements had a standard deviation of <2.6‰ ($n = 11$). The oxygen isotopic composition is given in the delta notation ($\delta^{18}O$) in per mille versus VSMOW.

3.6. Coupling compound-specific leaf wax δ^2H and sugar $\delta^{18}O$

The coupled $\delta^2H_{n\text{-alkane}}$–$\delta^{18}O_{sugar}$ approach (paleohygrometer) was previously described in detail by e.g. Hepp et al. (2015), Hepp et al. (2017), Hepp et al. (2019), Hepp et al. (2020), Hepp et al. (2021), Lemma et al. (2021) and Tuthorn et al. (2015). The fundamental assumption of the approach is that the isotopic composition of leaf water can be reconstructed by applying biosynthetic fractionation factors (ε_{bio}) on the measured $\delta^2H_{n\text{-alkane}}$ and $\delta^{18}O_{sugar}$ values. For $\delta^2H_{n\text{-alkane}}$ a constant ε_{bio} value of about −160‰ (Liu and Liu, 2019; Sachse et al., 2012; Sessions et al., 1999) is applied; for $\delta^{18}O_{sugar}$ the ε_{bio} value is assumed to be +27‰ (Cernusak et al., 2003; Gessler et al., 2009; Hepp et al., 2021; Schmidt et al., 2001; Sternberg et al., 1986; Yakir and DeNiro, 1990). This can be illustrated in a δ^2H–$\delta^{18}O$ diagram where the distance of the reconstructed leaf water to the global meteoric water line (GMWL) is defined as deuterium-excess (Dansgaard, 1964) (Fig. 2). We acknowledge that changes in the vegetation composition potentially lead to variations in ε_{bio} for both $\delta^2H_{n\text{-alkane}}$ (up to ~40–50‰) and $\delta^{18}O_{sugar}$ (up to ~5–8‰) (Gamarra et al., 2016; Lehmann et al., 2017; Sternberg, 1989), but previous studies highlight that the coupled $\delta^2H_{n\text{-alkane}}$–$\delta^{18}O_{sugar}$ approach enables a more robust reconstruction of the isotopic composition of the plants-source water and relative humidity (e.g., Hepp et al., 2020; Hepp et al., 2021) in comparison to single water isotope approaches.

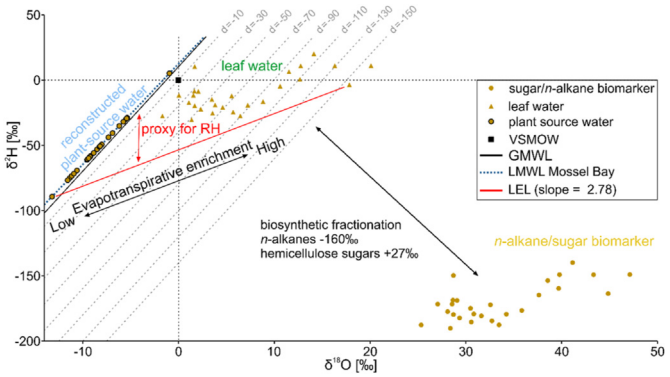

Fig. 2. *Coupled $\delta^2H_{n\text{-alkane}}$–$\delta^{18}O_{sugar}$ approach (paleohygrometer) displayed as δ^2H–$\delta^{18}O$ diagram showing the δ^2H of n-alkanes (weighted mean of C_{29} and C_{31}) and $\delta^{18}O$ of sugar (xylose) biomarkers, the reconstructed leaf and plant-source water, the global meteoric water line (GMWL, black line), and the local meteoric water line (LWML) from Mossel Bay (blue dashed line; Braun et al., 2017). The black double arrows indicates natural processes of evapotranspirative enrichment of leaf water along local evaporation lines (LEL; red line) and biosynthetic fractionation during biomarker synthesis, respectively. Grey dashed lines indicate the deuterium-excess, which can be used as proxy for relative humidity (red double arrow).* (For interpretation of the references to colour in this figure legend, the reader is referred to the Web version of this article.)

The concept is furthermore based on the fact that the isotopic composition of precipitation plots typically close to the GMWL ($\delta^2H_p = 8 \cdot {}^{18}O_p + 10$; Dansgaard, 1964). However, on the central southern Cape coast of South Africa, a local meteoric water line (LMWL) slightly deviating from the GMWL was described by Braun et al. (2017) ($\delta^2H = 7.70 \cdot \delta^{18}O + 12.10$). This LMWL was used for our calculations. We calculated equilibrium fractionation factors according to Horita and Wesolowski (1994) based on modern MAT, i.e. 16.4 °C (DWD Climate Data Center, 2020), resulting in 82.1‰ for ^2H and 10.0‰ for ^{18}O. The kinetic fractionation factor for ^2H and ^{18}O is set to 25.1‰ and 28.5‰, respectively (Merlivat, 1978). This yields a specific slope for a local evaporation line (LEL) of 2.78. The intercept of the LEL and the LMWL is the isotopic composition of reconstructed plant-source water (δ^2H and $\delta^{18}O$) (Fig. 2). The difference between deuterium-excess of the reconstructed leaf water and reconstructed plant-source water is then used to estimate the relative humidity (RH) for each sample (Fig. 2).

4. Results

4.1. Lithology and chronology

The composite sediment record from Vankervelsvlei, consists of five lithological units derived from distinct changes in sediment colour and physical properties (Fig. 3). Unit A from 15.0 to 13.0 m composite depth consists nearly exclusively of sand (89–90%) and has a low organic matter content (TOC: 0.05–3.3%) (Supplementary Information; Figs. S2 and S3). We observed that humic-rich water

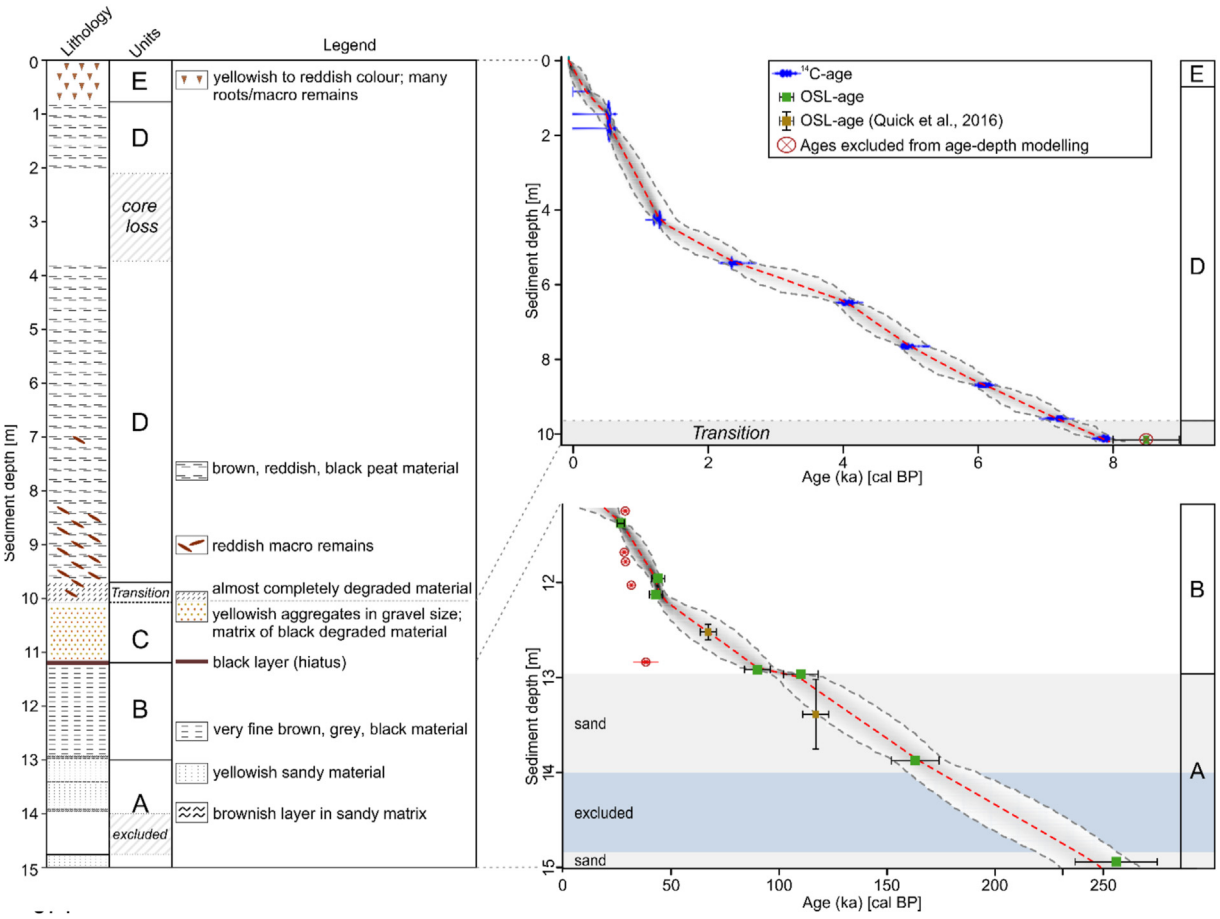

Fig. 3. Left: Lithology of the VVV16 composite record from Vankervelsvlei. Right: Age-depth models of the sediment record from Vankervelsvlei. Lithological units are shown on the right. Calibrated radiocarbon ages are displayed as probability density functions of the 2σ distributions. OSL ages are shown as boxes including 1σ error bars. Calibration and age-depth modelling was carried out using the R software package Bacon 2.4.3 (Blaauw and Christen, 2011). Please note that ^{14}C and OSL ages excluded from age-depth modelling are marked by a red circle with a red cross (see section 5.1 for more details). For comparison and confirmation of our age-depth model two OSL ages from sediment core VVV10.1 (Quick et al., 2016) including age (1σ horizontal error bars) and depth uncertainty (vertical error bars) are also depicted, but were not used for age-depth modelling. (For interpretation of the references to colour in this figure legend, the reader is referred to the Web version of this article.)

penetrated into the core section from 14.8 to 14.0 m composite depth between coring drives and those sediments were therefore excluded for biogeochemical analyses. However, the bottom of Unit A (15.0–14.8 m composite depth) was considered to be suitable for OSL dating. The remaining parts of Unit A, i.e. 15.0 to 14.8 m composite depth and 14.0 to 13.0 m composite depth, have a yellowish colour and two brownish layers within a sandy matrix at 14.0 and 13.3 m composite depths are notable (Fig. 3). Unit B from 13.0 to 11.18 m composite depth has a dark brown, dark grey and/or blackish colour and consists of very fine material (clay: 7–21%, silt: 61–90%) and has a higher organic matter content than Unit A (1.3–7.1%). A ~1 cm thick black layer marks the transition from Unit B to C at 11.18 m composite depth. This has been found in all sediment cores hitherto recovered from Vankervelsvlei, including earlier studies (e.g. Quick et al., 2016), and allows parallelisation of the sediment cores. Unit C and the transition to Unit D contains gravel-sized yellowish and reddish aggregates in a fine matrix. The transition zone to Unit D itself (10.32–9.68 m composite depth) is composed of dark brown, almost completely degraded, organic-rich material with some yellowish aggregates. Unit C and the transition to Unit D likely consist of reworked (soil) material (Strobel et al., 2019) and thus were both excluded from paleoenvironmental reconstruction. Unit D from 9.68 to 0.8 m composite depth consists of dark brown, reddish to black peat material (TOC: 48–54%). In the lower parts of Unit D, several reddish organic macro remains are present. Sediments are missing between 3.9 and 2.0 m depth, due to core loss during recovery. Sediments from Unit E from 0.8 to 0 m composite depth consist of well-preserved organic material (TOC: 45–46%) including roots and macro remains and are of yellowish to reddish colour (Fig. 3).

The chronology of the lower part of the sediment sequence (Units A and B; 15.0 to 11.18 m composite depth) shows stratigraphically consistent OSL ages and provides a basal age of 256 ± 19 ka (Fig. 3). Between Unit B and C (i.e. at 11.18 m composite depth), a sedimentary hiatus was inferred by Strobel et al. (2019), which is confirmed in this study (see section 5.1 for discussion). In the upper part of the sediment sequence, the 1σ uncertainties of an OSL age at the bottom of Unit D (i.e. 8.0 ± 0.5 ka in 10.15 to 9.95 m composite depth), which is not included in age-depth-modelling, overlaps with the ^{14}C-based chronology in this part of the sediment sequence (Fig. 3). ^{14}C ages of bulk TOC and organic macro particles in Units D and E are stratigraphically consistent and indicate higher sedimentation rates compared to the Units below (Fig. 3).

4.2. Element and isotope analyses as well as paleohygrometer approach

To provide the highest possible resolution, we extended the

previously published data by Strobel et al. (2019), i.e. elemental (Al, Fe) contents, $\delta^2H_{n\text{-alkane}}$, and $\delta^{13}C_{n\text{-alkane}}$ (n = 23) by new obtained data from this study (n = 128). Elemental contents of Al and Fe show low to intermediate values in Unit A (1520 ± 85 to 13,110 ± 740 ppm and 1040 ± 190 to 4150 ± 770 ppm, respectively), highest values in Unit B (27,500 ± 1400 to 76,800 ± 3800 ppm and 7300 ± 1400 to 16,400 ± 3000 ppm, respectively) and lowest values in Unit E (371 ± 21 to 2720 ± 150 ppm and 168 ± 31 to 2250 ± 420 ppm, respectively) (Fig. 4). Normalised XRF-scanning Fe counts follow the pattern of Al and Fe contents (Fig. 4). Strobel et al. (2019) ascribed Al variations to dust input coupled to varying wind at Vankervelsvlei based on the assumption that a fluvial transport of sediments to the coring position at the centre of the peatland is very unlikely as vegetation growing on the peatland acts like a filter for aquatic particle transport. Hence we use XRF-scanning Fe as high-resolution parameter whereas Al-counts are too low for interpretation.

$\delta^{13}C_{n\text{-alkane}}$ values have a wide range from −32.0 ± 0.1 to −28.0 ± 0.2‰ in Units A and B (Fig. 4). In Units D and E $\delta^{13}C_{n\text{-alkane}}$ values are generally more negative than in Units A and B (−33.0 ± 0.1 to −30.2 ± 0.1‰). $\delta^{13}C_{n\text{-alkane}}$ values mainly reflect past changes in the vegetation composition (C3, C4, CAM) (e.g. Diefendorf and Freimuth, 2017) and/or variations in C3 plants water use efficiency (WUE) (Farquhar et al., 1989; Hou et al., 2007).

In Units A and B, $\delta^2H_{n\text{-alkane}}$ values vary from −167.3 ± 3.8 to −139.9 ± 1.8‰. Marked shifts are present in Unit D and E (−190.5 ± 0.7 to −149.7 ± 0.6‰), which on average are associated with more negative $\delta^2H_{n\text{-alkane}}$ values than Units A and B. $\delta^{18}O_{sugar}$ values are more positive in Unit B (37.6 ± 0.6 to 47.1 ± 1.1‰) compared to Units D and E (25.3 ± 2.0 to 47.1 ± 1.2‰; Fig. 4). The results of the coupled $\delta^2H_{n\text{-alkane}}$-$\delta^{18}O_{sugar}$-approach (paleohygrometer) provide d-excess values from −143.4 ± 8.4 to −82.3 ± 4.0‰ in Unit B, and −88.6 ± 2.3 to −1.1 ± 0.6‰ in Units D and E (Fig. 6). Reconstructed plant-source water ranges from −89.3 to −29.4‰ for δ^2H and from −13.2 to −5.4‰ for $\delta^{18}O$ in Unit B, and from −76.8 to 5.0‰ and from −11.5 to −0.9 in Unit D and E, respectively. Reconstructed RH is lower in Unit B (17.8–50.1%) than in Units D and E (46.8–93%) (Fig. 4). Elemental contents (Al and Fe) and $\delta^2H_{n\text{-alkane}}$ show significant correlations (r = 0.82 to 0.83; α = 0.05, Fig. S4) and Fe also significantly correlates with reconstructed plant-source water (r = 0.53; α = 0.05, Figs. 4 and S4).

Based on modern isotopic variability in rainfall, we anticipate that changes in reconstructed plant-source water ($\delta^{18}O$ and δ^2H) reflect changes in the isotopic composition of precipitation related to changes in the precipitation source, i.e. i) Westerlies (Atlantic Ocean), ii) Easterlies (Indian Ocean) and iii) local sources (Strobel et al., 2020). Reconstructed RH reflects growing season air RH (Hepp et al., 2021; Strobel et al., 2020). This leads to the assumption that RH is higher during phases of generally (year-round) and/or seasonally moist conditions, whereas during periods of low RH conditions were either generally drier and/or precipitation seasonality was increased, i.e. the reduction of either summer or winter precipitation. Similar to $\delta^2H_{n\text{-alkane}}$, $\delta^{18}O_{sugar}$ records the isotopic composition of precipitation but is more prominently modulated by evapotranspirative enrichment (Strobel et al., 2020; Struck et al., 2020) and thus is a sensitive proxy for changes in the precipitation-evaporation balance at Vankervelsvlei.

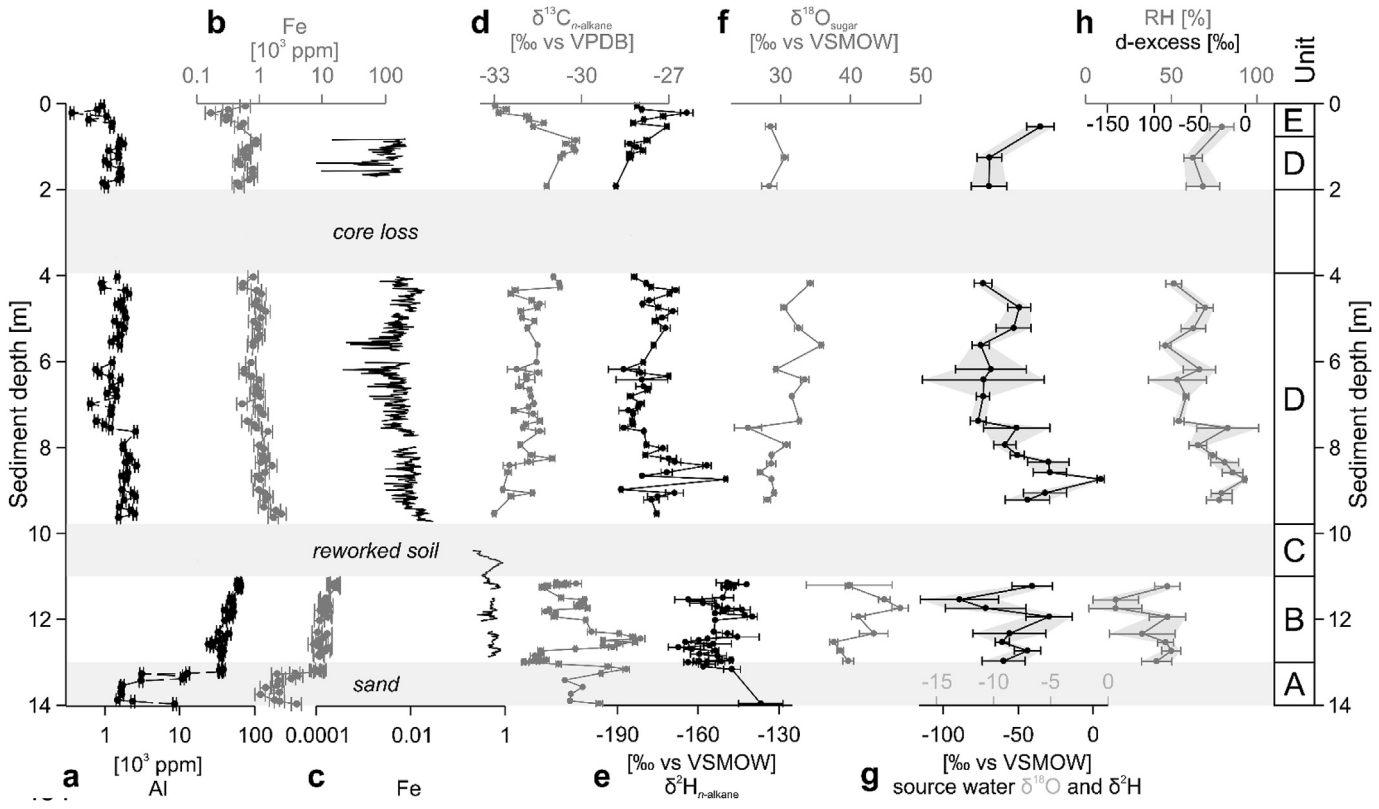

Fig. 4. a) Al and b) Fe contents, c) normalised Fe, d) $\delta^{13}C_{n\text{-alkane}}$, e) $\delta^2H_{n\text{-alkane}}$ and f) $\delta^{18}O_{sugar}$ as well as g) the isotopic composition of the reconstructed source water, h) d-excess and relative humidity derived from the coupled isotope approach from the VVV16 sediment sequence. Error bars and the grey shaded area in g) and h) indicate expanded uncertainties derived from the uncertainty propagation law. Lithological units are depicted at the right. Note Log_{10} scale for a), b) and c).

5. Discussion

5.1. Chronostratigraphy

The basal age of 256 ± 19 ka of the sediment sequence from Vankervelsvlei is in the range of the dunes underlying and surrounding Vankervelsvlei, i.e. 205 to 250 ka BP (Bateman et al., 2011) (Table S4) and indicates that the depression hosting Vankervelsvlei today was probably formed contemporaneously, implying that we have now recovered the entire sedimentary sequence at this site. However, due to the infiltration of humic-rich water into the core section from 14.8 to 14.0 m composite depth between coring drives, those sediments had to be excluded from paleoenvironmental reconstruction. Bulk TOC ^{14}C ages published in a previous investigation from Vankervelsvlei (Strobel et al., 2019) showed a distinct offset to the revised OSL-based age-depth model presented here (Fig. 3). As these ^{14}C ages of bulk TOC are close to the dating limit of ^{14}C only minor amounts of young carbon likely bias these dating results (e.g., Briant and Bateman, 2009). At Vankervelsvlei, we hypothesise that percolating waters containing leached organic carbon may account for the too young bulk ^{14}C ages. Additionally, two brownish layers at 14.0 and 13.3 m composite depth are likely a result of this percolating water (Fig. 3). Mandiola et al. (2021) analysed the age of water at several depths within the Vankervelsvlei deposits, revealing modern ^{14}C ages for water in deeper layers (~6.3 m below surface). Although dissolved organic matter was not analysed in that study, the presence of percolating water supports our aforementioned hypothesis of contamination of the bulk radiocarbon ages. ^{14}C ages in the Vankervelsvlei study by Quick et al. (2016) were not in stratigraphic order and were distinctly offset from OSL ages, further supporting our hypothesis. Vertical (re-)deposition of carbon in sediments leading to biased ^{14}C ages was also recently observed by e.g. Briant et al. (2018), Colarossi et al. (2020) and Palstra et al. (2021), but the new stratigraphically consistent OSL data presented here now provide robust age information for this part of the record.

In the upper part of Unit B, the chronology implies a sedimentary hiatus at 11.18 m sediment depth. The hiatus was previously ascribed to desiccation from 28,050 $^{+510}/_{-600}$ to 8,360 $^{+730}/_{-810}$ cal BP (Strobel et al., 2019). Considering modelling and dating uncertainties within the framework of the new OSL-based chronology, we can confirm this sedimentary hiatus during MIS 2 and the transition to MIS 1 (20.3 $^{+5.2}/_{-14}$ ka to 7230 $^{+160}/_{-210}$ cal BP). This is consistent with reconstructions of relatively dry conditions identified in regional archives (see section 5.2.1 for detailed discussion). After the deposition of reworked soil material in Unit C and the transition to Unit D (likely in MIS 2 and/or the Early-Holocene), continuous sedimentation began in the Middle-Holocene, i.e. 7230 $^{+160}/_{-210}$ cal BP, lasting until present day (Fig. 3).

Several sediment cores have been recovered from different locations at Vankervelsvlei during the past decades (Irving and Meadows, 1997; Quick et al., 2016). However, the comparisons of those cores to the new composite record presented here is constrained by missing sections (especially in the youngest part), lithological inconsistencies and occasionally poor chronological control of the previous studies. Nevertheless, the sediment cores investigated by Quick et al. (2016) can roughly be parallelised to the lower part of our composite record (Units A and B). The stratigraphic location of an OSL age 117 ± 6 ka in core VVV10.1 (Quick et al., 2016) lies between our ages of 163 ± 11 and 110 ± 8.1 ka, further supporting our chronology (Fig. 3). Another OSL age of 67.2 ± 3.7 ka from core VVV10.1 (Quick et al., 2016) is also stratigraphically consistent with our record, being located between the two new OSL ages of 90 ± 6 ka and 43 ± 3 ka (Fig. 3). Unfortunately, it is not possible to better match records, inhibiting a precise inclusion of all VVV10.1 ages from Quick et al. (2016).

5.2. Paleoenvironmental- and climate evolution

5.2.1. Late Quaternary

The sediments lying between the two lowermost OSL-ages, i.e. 256 $^{+19}/_{-19}$ and 110 $^{+8}/_{-8}$ ka (late MIS 8 to early MIS 7 and MIS 5e), consist almost exclusively of sand, limiting paleoenvironmental inferences for this period. However, high sand contents likely indicate significant geomorphic activity at Vankervelsvlei area and within the surrounding area. This is consistent with studies of the history of dune formation within the Wilderness Embayment, and with two periods of barrier dune construction during MIS 6 and 5e, i.e. from 159 to 143 ka and from 130 to 120 ka, respectively (Bateman et al., 2011). Quick et al. (2016) reported that no pollen was preserved in these sandy sediments dating 140 to 115 ka at Vankervelsvlei, which is consistent with our record.

From 171 $^{+16}/_{-13}$ to 136 $^{+16}/_{-16}$ ka, $\delta^{13}C_{n\text{-alkane}}$ values imply a contribution from vegetation using CAM and/or C4 photosynthesis, and/or decreased moisture availability (water use efficiency; WUE) at Vankervelsvlei (Fig. 5). Typically, $\delta^{13}C_{n\text{-alkane}}$ values from −25 to −35‰ refer to C3 plants while C4 plants range from −15 to −20‰ and CAM plants show intermediate values (Boom et al., 2014; Carr et al., 2022; Diefendorf and Freimuth, 2017; Huang et al., 2006). Changes in the atmospheric CO_2 concentration may also impact $\delta^{13}C_{n\text{-alkane}}$ values over an order of 1–2‰ on glacial-interglacial timescales (Breecker, 2017; Hare et al., 2018; Schubert and Jahren, 2012; Voelker et al., 2016). *n*-Alkane concentrations in this unit were too low for $\delta^{2}H_{n\text{-alkane}}$ measurements to be used as an indicator of precipitation source. Similarly, elemental Fe is too low for interpretation and cannot be used for this period.

From 136 $^{+16}/_{-16}$ to 112 $^{+12}/_{-11}$ ka more positive $\delta^{13}C_{n\text{-alkane}}$ values, in comparison to the previous period, imply drier conditions and the presence of more plants using CAM and/or C4 photosynthetic modes. Although only a few samples that yielded sufficient *n*-alkanes for $\delta^{2}H_{n\text{-alkane}}$ measurements, the $\delta^{2}H_{n\text{-alkane}}$ values indicate a high contribution of Westerly-derived winter precipitation at this time. From 112 $^{+12}/_{-11}$ to 103 $^{+7}/_{-7}$ ka (MIS 5e, 5d), from 88 $^{+8}/_{-8}$ to 82 $^{+10}/_{-12}$ ka (MIS 5c, 5b) and from 42 $^{+2}/_{-2}$ to 39 $^{+4}/_{-5}$ ka (MIS 3) the $\delta^{13}C_{n\text{-alkane}}$ values clearly indicate a dominant contribution of plants using C3 photosynthesis. These periods are accompanied by more positive $\delta^{2}H_{n\text{-alkane}}$ values, indicting high contributions of both winter (Westerly-derived) and summer (Easterly-/locally-derived) precipitation and a likely year-round rainfall regime. In contrast, plants using CAM and/or C4 photosynthetic mode are present at Vankervelsvlei from 82 $^{+10}/_{-12}$ to 42 $^{+2}/_{-2}$ ka (MIS 5a to early MIS 3), from 39 $^{+4}/_{-5}$ to 20 $^{+5}/_{-12}$ ka (transition from MIS 3 to MIS 2) (Fig. 5). Contemporaneously, more negative $\delta^{2}H_{n\text{-alkane}}$ values indicate an increased Westerly-derived winter precipitation contribution. Unfortunately, the full suite of proxy data is not available between 103 $^{+7}/_{-7}$ and 88 $^{+8}/_{-8}$ ka due to a lack of samples.

Plant-source water ($\delta^{2}H$ and $\delta^{18}O$) and RH values show minor variations from MIS 5d to MIS 2, with a prominent shift from moist to very dry conditions at the transition from MIS 3 to MIS 2 (Fig. 5). Although the temporal resolution of these proxies is limited, this study demonstrates the applicability of the coupled $\delta^{2}H_{n\text{-alkane}}$–$\delta^{18}O_{sugar}$ approach (paleohygrometer) in sediments of Late Quaternary age. We acknowledge that the uncertainties of the proxies derived from the coupled $\delta^{2}H_{n\text{-alkane}}$–$\delta^{18}O_{sugar}$ approach should be focused in future studies. High-resolution elemental Fe data cannot be interpreted prior to MIS 5c, but indicate maxima in minerogenic inputs at the transitions from MIS 5b to 5a, MIS 4 to MIS 3 and MIS 3 to MIS 2, suggesting an increased importance of wind during these periods at Vankervelsvlei (Fig. 5). While

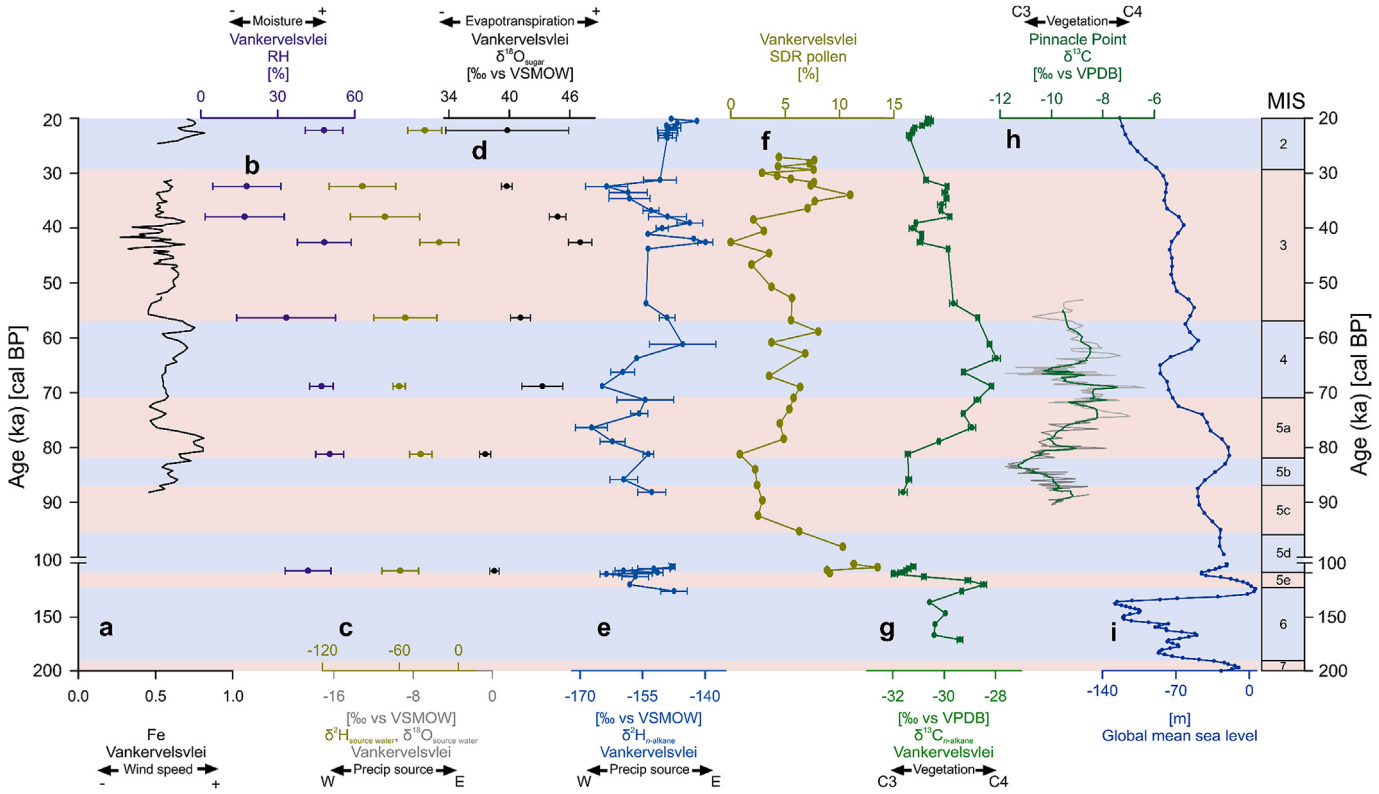

Fig. 5. Late Quaternary inorganic and organic down-core geochemistry of the VVV16 sediment record as indicators a) for wind (Fe), b) relative humidity (RH; moisture), c), e) precipitation source (W = Westerlies, E = Easterlies and/or local sources), d) evapotranspiration and g) vegetation composition and/or C3 plants water use efficiency. For comparative purposes f) percentages of succulent/drought resistant (SDR) pollen from Vankervelsvlei are shown (Quick et al., 2016). Note that these pollen results are from an earlier study on VVV and are plotted on their original independent age scale. Additionally, (supra-)regional paleoenvironmental records are plotted: h) $\delta^{13}C$ from Pinnacle point (grey line original data; coloured line running mean of eleven data points) (Bar-Matthews et al., 2010) and i) Global mean sea level (Waelbroeck et al., 2002). Marine Isotope Stages (MIS (Lisiecki and Raymo, 2005)) are shown on the right. See Fig. 1 for location of the studies. Note axis break at 100 ka.

minerogenic input is low during phases of dominant Westerly-derived winter precipitation, it increases during periods in which we observe precipitation contributions from both Westerly- and Easterly/locally-derived precipitation. This indicates a potential relationship between wind-driven minerogenic and Easterly/locally-derived precipitation (Fig. 5).

Trends in $\delta^{13}C_{n\text{-alkane}}$ from this study correspond well with changes in the occurrence of Succulent/Drought Resistant (SDR) pollen (Fig. 5g) from sediment core VVV10.1 (Quick et al., 2016). The SDR pollen sum is dominated by *Euphorbia* and was previously interpreted to indicate local drought at Vankervelsvlei (Quick et al., 2016). Distinctly more negative $\delta^{13}C_{n\text{-alkane}}$ values and low SDR pollen imply greater moisture availability and limited rainfall seasonality from 88 $^{+8}/_{-8}$ to 82 $^{+10}/_{-12}$ ka (MIS 5c, 5b) (year-round-rainfall regime). Accordingly, more positive $\delta^{13}C_{n\text{-alkane}}$ values and a higher SDR pollen sum imply drier conditions and increased rainfall seasonality from 82 $^{+10}/_{-12}$ to 42 $^{+2}/_{-2}$ ka (MIS 5a to MIS 3). From 42 $^{+2}/_{-2}$ to 37 $^{+5}/_{-5}$ ka (MIS 3), more negative $\delta^{13}C_{n\text{-alkane}}$ values and lower SDR pollen indicate a return to moist and less seasonal conditions. This is followed by a trends towards more positive $\delta^{13}C_{n\text{-alkane}}$ values and higher SDR pollen percentages, indicating drier conditions from 37 $^{+5}/_{-5}$ to 20 $^{+5}/_{-12}$ ka (transition from MIS 3 to MIS 2) (Fig. 5).

Several speleothem records have been presented for the southern Cape YRZ during the past decades. However, data gaps limit comparability with our record for MIS 6 to MIS 5d. Notwithstanding more positive $\delta^{13}C$ values at Pinnacle Point suggest dry conditions during early MIS 6 followed by even more positive $\delta^{13}C$ values, indicating even drier conditions in MIS 5e at the site (Staircase Cave; ~80 km SW of Vankervelsvlei; Braun et al., 2019), which is in good agreement with our data. An additional record from Pinnacle Point (PP29; Braun et al., 2020) implies moist conditions from MIS 5d to MIS 5b due to negative $\delta^{13}C$ values. Most records show initial and/or continuing speleothem growth after ~90 ka and provide climate information in high temporal resolution, e.g. at Herolds Bay Cave, Pinnacle Point (Crevice Cave, PP29) and Efflux Cave (respective locations: ~50 km SW, ~80 km SW and ~100 km NW of Vankervelsvlei) (see Fig. 1C for location) (Bar-Matthews et al., 2010; Braun et al., 2019, 2020). Although the temporal resolution of the Vankervelsvlei record is lower than at these sites, $\delta^{13}C$-records from the speleothems closely resemble the $\delta^{13}C_{n\text{-alkane}}$ trends from Vankervelsvlei (Fig. 5). Together, these records provide a reasonably coherent environmental picture at the southern Cape coast whereby more vegetation using CAM and/or C4 photosynthetic mode occurred during MIS 4 compared to MIS 5b and MIS 3 (Fig. 5). Unfortunately, comparison of our proxies for precipitation source to $\delta^{18}O$ data from speleothem records is limited because it is challenging to disentangle the effects of temperature and precipitation source in the latter (e.g. Braun et al., 2019 and discussion therin). Overall, several paleoclimate records located at or near the present day southern Cape coast show relatively coherent trends with evidence from several proxies indicating (supra-)regional driving forces leading to the observed pattern during the Late Quaternary.

The pattern of our $\delta^{2}H_{n\text{-alkane}}$-record also resembles changes in the global mean sea level (GMSL) (Waelbroeck et al., 2002, Fig. 5) indicating changes in precipitation sources on glacial-interglacial scale. More positive $\delta^{2}H_{n\text{-alkane}}$ values indicate a high contribution

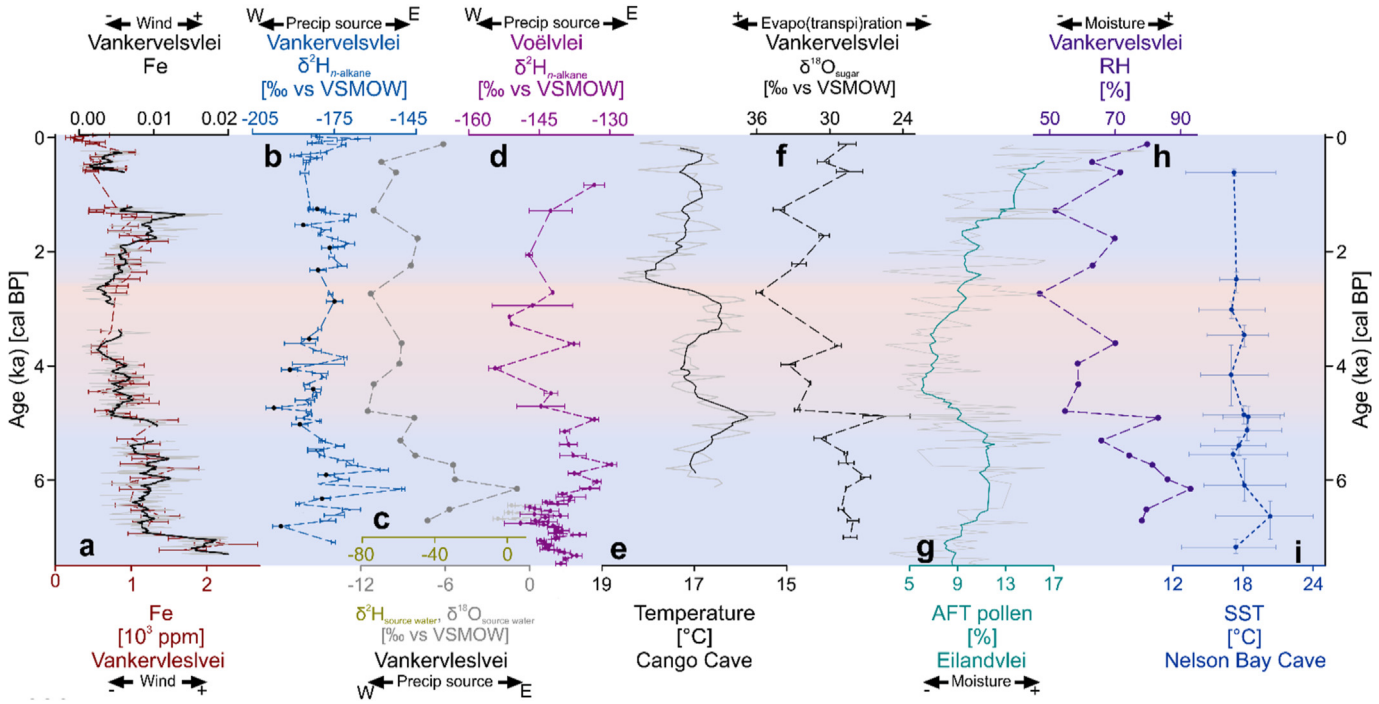

Fig. 6. Inorganic and organic geochemistry of the VVV16 sediment record (a, b, c, f, h) as proxies for wind, precipitation source (W = Westerlies, E = Easterlies and/or local sources), evapotranspiration (note inverse axis) and relative humidity (moisture). Black dots in b indicate results from Strobel et al. (2019). For comparative purposes regional paleoenvironmental records are plotted on their original independent age scale: d) $\delta^2H_{n\text{-alkane}}$ from Voëlvlei indicating precipitation source (Strobel et al., 2021), e) terrestrial paleotemperatures at Cango Cave (note inverse axis) (Talma and Vogel, 1992), g) Afrotemperate forest (AFT) pollen from Eilandvlei indicating moisture (Quick et al., 2018), and i) sea surface temperature (SST) from Nelson Bay Cave (Cohen, 1993; Cohen and Tyson, 1995). For e), g) and h) grey line indicates original data and colour line is the running mean of seven and eleven data points, respectively. See Fig. 1 for location of the studies. (For interpretation of the references to colour in this figure legend, the reader is referred to the Web version of this article.)

of Easterly- and/or locally-derived precipitation during high sea level (interglacial periods) and negative $\delta^2H_{n\text{-alkane}}$ values occur during low sea level low (glacial periods) indicating high proportions of Westerly-derived precipitation (Waelbroeck et al., 2002, Fig. 5). However, the ocean as a precipitation source becomes isotopically enriched during glacial periods due to the so called 'ice effect' (Dansgaard, 1964; Friedman et al., 1964), which is opposed to our observed pattern and therefore dampens the magnitude in our $\delta^2H_{n\text{-alkane}}$-record from Vankervelsvlei.

Additionally, during glacial periods, sea level was distinctly lower than at present, with the coastline south of its present position, increasing continentality at Vankervelsvlei (Cawthra et al., 2014, 2021; Strobel et al., 2019). This was likely most pronounced during MIS 6 and MIS 2 (~90–100 km) and to a lesser degree during MIS 4 (~20–30 km) (BODC, 2014; Cawthra et al., 2014; Lisiecki and Raymo, 2005; Waelbroeck et al., 2002). We therefore suggest that variations in the GMSL are a distinct driver of climate variability at the southern Cape coast leading to increased continentality and drier conditions during glacial compared to interglacial periods. This is consistent with the absence of peat accumulation at Vankervelsvlei during MIS 2 (discussed below).

The hiatus from 20 $^{+5}/_{-12}$ ka to 7,330 $^{+200}/_{-230}$ cal ka BP likely indicates drought conditions at Vankervelsvlei, leading to desiccation and degradation of the previously accumulated peat during MIS 2 (Quick et al., 2016; Strobel et al., 2019). Drier conditions during MIS 2 were also found for example at Rietvlei, ~150 km to the west of Vankervelsvlei (Quick et al., 2015) supporting our interpretation at Vankervelsvlei. During MIS 2, sea level was lower than present, i.e. ~123 m b.s.l., which led to an exposure of the Paleo-Agulhas Plain, and thus continentality at Vankervelsvlei distinctly increased due to migration of the coastline up to ~90 km south of its present position (BODC, 2014; Cawthra et al., 2014; Cawthra et al., 2021; Waelbroeck et al., 2002). Modelled temperatures and precipitation (seasonality) imply lower mean annual temperatures (i.e. 2–4 °C), and reduced precipitation, due to increased continentality of this area, resulting in overall dry conditions during MIS 2 (Engelbrecht et al., 2019). There is one speleothem record from Cango Cave for the southern Cape coast covering the LGM, which also shows a distinct hiatus during parts of MIS 2 and the early Holocene (i.e. from 16,660 to 6110 cal BP) (Talma and Vogel, 1992) contemporaneous with the dry conditions inferred from the hiatus. Hence, conditions during MIS 2 at the southern Cape were likely distinctly drier than during the past ~110 $^{+13}/_{-11}$ ka when peat accumulation likely started at Vankervelsvlei. Conversely, both proxy (e.g. Chase et al., 2017; Chase and Meadows, 2007) and modelled data (e.g. Cockcroft et al., 1987; Engelbrecht et al., 2019) indicate moister conditions in the interior and at the south-north aligned Cape Fold Mountains and the western escarpment of South Africa inter alia due to reduced temperatures leading to an increased effective ecosystem moisture availability.

5.2.2. Holocene

5.2.2.1. Middle- and Late-Holocene. According to the slightly positive $\delta^{18}O_{sugar}$ values, evapotranspiration is low from 7230 $^{+160}/_{-210}$ to 4890 $^{+280}/_{-180}$ cal BP (Fig. 6). More positive values of $\delta^2H_{n\text{-alkane}}$ and plant-source water as well as high RH values indicate distinct precipitation contributions from tropical Easterlies and/or local sources and moist conditions year-round. Contemporaneously, high Fe values likely indicate wind induced minerogenic input at Vankervelsvlei. We therefore suggest that wind induced minerogenic input increases when precipitation contribution from Easterlies and local sources is high.

From 4890 $^{+280}/_{-180}$ to 2710 $^{+590}/_{-310}$ cal BP, increased Westerly-derived precipitation is indicated by more negative values of $\delta^2H_{n\text{-alkane}}$ and reconstructed plant-source water. During this period, RH is low and positive $\delta^{18}O_{sugar}$ values indicate high evapotranspirative enrichment, which likely implies dry summer conditions, and a reduced or absent precipitation contribution from the Easterlies and/or local sources. Low elemental Fe values point to less wind induced minerogenic input, which again seems to be coupled with low precipitation contribution from Easterlies and/or local sources (Fig. 6).

From 2710 $^{+590}/_{-310}$ cal BP until present day, variable, but overall more positive values of reconstructed plant-source water and increased RH likely imply an increased precipitation contribution from Easterlies and/or local sources and overall moist conditions, comparable to present day. This is underlined by a trend to less positive $\delta^{18}O_{sugar}$ values indicating low evapotranspirative enrichment (Fig. 6). High-resolution $\delta^2H_{n\text{-alkane}}$ and Fe values follow the aforementioned trend, but show a further short period of distinctly increased Easterly-derived summer precipitation contribution accompanied by increased wind induced minerogenic input from 2,350$^{+290}/_{-190}$ to 1,210 $^{+240}/_{-140}$ cal BP. In the uppermost parts of the record, highly variable conditions are derived from distinct changes in $\delta^2H_{n\text{-alkane}}$ and Fe values (Fig. 6).

During the Holocene, the pattern of RH tracks the abundance of Afrotemperate forest (AFT) pollen recorded at neighbouring lake Eilandvlei, located ~25 km to the west of Vankervelsvlei (Figs. 1C and 6). The AFT pollen signal is an indicator for moisture availability for the surrounding Wilderness area, including Vankervelsvlei, being in line with other moisture indicators from Eilandvlei (Quick et al., 2018; Wündsch et al., 2018). The correspondence between RH and AFT pollen suggests a consistent moisture signal in the Wilderness area during the Holocene. Plant-source water and $\delta^2H_{n\text{-alkane}}$ suggest that these moist conditions are related to increased precipitation contributed during summer (Easterlies) and/or from local sources. Conversely, dry conditions are associated with less precipitation contribution during summer (Easterlies) and/or from local sources.

At Voëlvlei, ~80 km west of Vankervelsvlei, the $\delta^2H_{n\text{-alkane}}$ record also mirrors changes in the precipitation source (Strobel et al., 2021) (Fig. 6d). The overall pattern at this site suggested a contribution of i) both Westerly- and Easterly/locally-derived precipitation (8,230 $^{+250}/_{-260}$ to 6,410 $^{+140}/_{-440}$ cal BP), ii) dominant Easterly/local precipitation (6,410 $^{+140}/_{-440}$ to 4700 $^{+500}/_{-230}$ cal BP), is followed by iii) variable precipitation contribution but a trend from Westerly-to Easterly-dominance (4700 $^{+500}/_{-230}$ cal BP to present day) (Strobel et al., 2021). This pattern is consistent with the findings from Vankervelsvlei and Eilandvlei providing a consistent climate picture of the coastal sites at South Africa's southern Cape coast.

Holocene terrestrial temperature and sea surface temperature (SST) records are hitherto very rare at South Africa's southern Cape coast. Overall, the pattern of the $\delta^{18}O_{sugar}$ at Vankervelsvlei resembles the terrestrial temperature record from Cango Cave (Talma and Vogel, 1992) likely indicating high (low) evapotranspiration at Vankervelsvlei contemporaneous with high (low) temperatures at Cango Cave during the Middle- and Late-Holocene (Fig. 6). Additionally, two minor trends towards more Westerly-derived winter precipitation ($\delta^2H_{n\text{-alkane}}$ and source water) at Vankervelsvlei (at 4,710 $^{+310}/_{-290}$ and 2,710 $^{+590}/_{-310}$ cal BP) are accompanied by distinctly decreased temperatures at Cango Cave, while during phases of increased precipitation contribution from Easterlies and/or local sources at Vankervelsvlei temperatures are increased at Cango Cave (Fig. 6). While the variable trend in evapotranspiration at Vankervelsvlei from ~3 cal ka BP until present day is also mirrored in variable temperatures at Cango Cave, the increasing trend towards moister conditions cannot be related to changes in temperature during this period (Fig. 6). Although the SST-record from Nelson Bay Cave (NBC, (Cohen and Tyson, 1995), Fig. 1C) indicates higher SST at ~6,640 $^{+400}/_{-270}$ cal BP and ~4900 $^{+220}/_{-190}$ cal BP, which might be related to high RH and high precipitation contribution from Easterlies and/or local sources at Vankervelsvlei, analytical and chronological uncertainties as well as low temporal resolution all limit the comparability of this record to our study. However, both temperature records from Cango Cave and Nelson Bay Cave indicate that terrestrial temperatures and SST might be a driver of moisture at Vankervelsvlei during the Holocene. Higher temperatures might yield distinct land-sea gradients fostering onshore flows of moist air masses from local sources to the coastal areas during the Holocene, accounting for the aforementioned pattern in moisture and precipitation sources at Vankervelsvlei and surrounding coastal areas. The presence of onshore flows was previously postulated at Vankervelsvlei by increased strontium (Sr) contents, which originate largely from sea spray (Strobel et al., 2019), based on the results of the present study, we suggest that precipitation contribution from local sources distinctly contributes to moisture at the southern Cape coastal sites. Sites located further inland are at higher elevations due to the southern Cape's morphology, and precipitation from local sources is therefore likely limited compared to the coastal sites. This implies changes in moisture availability at coastal and inland sites, e.g. Seweweekspoort (Chase et al., 2017), might be independent. Thus, these new data add further weight to the proposed steep climate response gradient between coastal and uplands sites in the southern Cape region (Chase et al., 2020; Chase and Quick, 2018). However, to provide more detailed information about those land-sea interactions, there is a need for more continuous high-resolution quantitative sea-surface and terrestrial temperatures at South Africa's southern Cape coast.

5.2.2.2. 600 cal BP until present. There is a significant correlation between minerogenic input (Fe contents) from our study and aquatic/riparian pollen percentages ($r = 0.68$, $\alpha = 0.05$, Figs. 7 and S4), derived from the uppermost section of the same Vankervelsvlei sediment sequence (1.96–0 m composite depth; 595 $^{+120}/_{-65}$ cal BP to present day) by du Plessis et al. (2021). The aquatic/riparian pollen are dominated by local Haloragaceae pollen (most likely *Myriophyllum*, a freshwater aquatic plant (du Plessis et al., 2021)). Based on pollen analyses only, du Plessis et al. (2021) previously argued that low Haloragaceae pollen abundances might indicate high water levels at Vankervelsvlei. This interpretation was largely based on this taxon's relation to variations in Cyperaceae pollen. In light of the fact that wind-induced minerogenic input (Fe) has been associated with high precipitation from Easterlies and/or local sources under relatively moist year-round rainfall conditions (Strobel et al., 2019), we apply the same interpretation for the last 595 $^{+120}/_{-65}$ cal BP here. We therefore suggest that high Haloragaceae pollen indicate higher water levels at Vankervelsvlei. This is in line with previous assertions that increases in the presence of Haloragaceae is associated with high water stands in other South African lakes (e.g. Howard-Williams, 1979; Neumann et al., 2008). The pattern of minerogenic input (Fe) and aquatic/riparian pollen is mirrored by the trends in the Afrotemperate forest (AFT) pollen sum, which has previously been interpreted to indicate increased year-round and less seasonal moisture conditions at Vankervelsvlei (du Plessis et al., 2021) and the surrounding Wilderness area (Quick et al., 2018). According to this interpretation, moister conditions peak at ~595 $^{+120}/_{-65}$, ~530 $^{+70}/_{-100}$ and ~260 $^{+85}/_{-160}$ cal BP. In general, our parameters lack the resolution (due to core loss) to characterise the Medieval Climate Anomaly (~950-700 cal BP), but they do show a trend towards drier conditions during the Little Ice

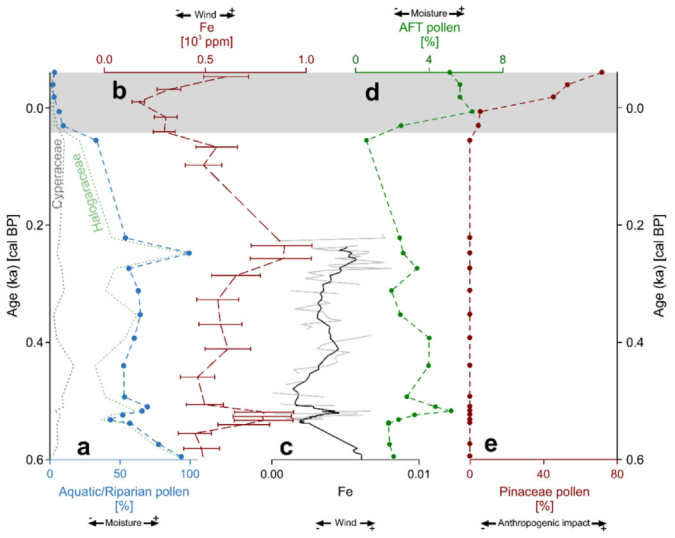

Fig. 7. a) Aquatic/riparian pollen indicative for water table variations (du Plessis et al., 2021), b) and c) Fe contents and counts as local wind indicators, d) Afrotemperate forest (AFT) pollen indicative for moisture and e) Pinaceae and pollen representing anthropogenic impact (du Plessis et al., 2021). The grey shaded area marks the presence of anthropogenic impact at Vankervelsvlei indicated by increasing Pinaceae pollen, which explains fading similarities between a, b and d.

Age (~650-300 cal BP) (Figs. 6 and 7). Anthropogenic impacts, i.e. forestry (Pinaceae pollen), began to alter the landscape (and site) after 60 $^{+130}/_{-90}$ cal BP, which explains the fading similarities in proxies in the uppermost parts of the record (Fig. 7).

6. Conclusions

Our multi-proxy record from Vankervelsvlei provides new insights into the paleoclimate history at South Africa's southern Cape Coast during the Late Quaternary. In this specific region Vankervelsvlei represents a scarce terrestrial archive in that it was not influenced by the intrusion of marine water, enabling more robust paleoclimatic reconstructions. The age model based on the OSL and ^{14}C-based chronologies produces a basal age of 263 ± 19 ka, and dry conditions likely prevailed from this time to 136 $^{+16}/_{-16}$ ka at Vankervelsvlei. This is contemporaneous with a major phase of barrier dune construction in the surrounding areas, particularly during MIS 5e. Even drier conditions and low geomorphic activity at the site occurred from 136 $^{+16}/_{-16}$ to 112 $^{+12}/_{-11}$ ka. From 112 $^{+12}/_{-11}$ to 103 $^{+7}/_{-7}$ ka, from 88 $^{+8}/_{-8}$ to 82 $^{+10}/_{-12}$ ka and from 42 $^{+2}/_{-2}$ to 39 $^{+4}/_{-5}$ ka. $\delta^{13}C_{n\text{-alkane}}$ values indicate a contribution largely from plants using C3 photosynthesis, but with an increased contribution of plants using CAM and/or C4 photosynthesis from 82 $^{+10}/_{-12}$ to 42 $^{+2}/_{-2}$ ka and from 39 $^{+4}/_{-5}$ to 20 $^{+5}/_{-12}$ ka.

An increased Westerly-derived winter precipitation contribution is suggested by more negative $\delta^2H_{n\text{-alkane}}$ values from 120 $^{+15}/_{-14}$ to 105 $^{+9}/_{-8}$ ka, from 79 $^{+11}/_{-13}$ to 76 $^{+11}/_{-12}$ ka and from 68 $^{+13}/_{-12}$ to 66 $^{+14}/_{-11}$ ka. Greater contributions of Easterly-derived summer precipitation are implied by more positive $\delta^2H_{n\text{-alkane}}$ values from 74 $^{+12}/_{-13}$ to 71 $^{+13}/_{-13}$ ka and 64 $^{+13}/_{-11}$ to 37 $^{+5}/_{-5}$ ka. Variable contributions of both Westerly- and Easterly-derived precipitation are evident from 37 $^{+5}/_{-5}$ to 20 $^{+5}/_{-12}$ ka.

High-resolution analyses of the Middle- and Late-Holocene parts of the record show three distinct phases. The first phase from 7230 $^{+160}/_{-210}$ to 4890 $^{+280}/_{-180}$ cal BP is characterised by moist conditions and year-round rainfall, including a distinct contribution from mainly locally-derived summer-precipitation. From 4890 $^{+280}/_{-180}$ to 2840 $^{+350}/_{-330}$ cal BP, dry conditions and higher seasonality, with largely Westerly-derived winter precipitation, occurred. After 2840 $^{+350}/_{-330}$ cal BP, moisture has been variable, but overall increasingly accompanied by locally-derived summer-precipitation, leading to a year-round rainfall regime again.

These new data are in line with previous investigations at Vankervelsvlei and closely located stalagmite records, providing a coherent regional climate signal at the southern Cape coast of South Africa. Due to distinct sea-level variations during the Late Quaternary, the coastline likely migrated up to 100 km south of its present position during glacial periods leading to increased continentality and drier conditions at Vankervelsvlei. Sea-level is therefore a distinct driver of near-coastal climate variability on orbital time scales. During the Middle- and Late-Holocene, Vankervelsvlei provides consistent climate signals compared to published coastal archives along South Africa's southern Cape coast. There are still differences in the climatic trajectories between coastal and inland sites, possibly due to the application of indirect hydrological proxies at the latter and thus limited proxy comparability. On the coast, local sources are hypothesised to distinctly contribute to the precipitation and moisture pattern, coupled with distinct (sea-surface) temperature driven onshore winds. Further studies are needed to more fully explore the validly of this hypothesis. Additionally, our study highlights that future studies should focus on the investigation of both water isotopes, i.e. $\delta^{18}O$ and δ^2H, to i) enable proxy comparability and ii) overcome distinct uncertainties related to single-water-isotope studies, and therefore allow more robust paleohydrological reconstructions.

Data availability statement

Data used in this study is available on PANGAEA via https://doi.pangaea.de/10.1594/PANGAEA.940148.

Author contribution

Paul Strobel: Conceptualization, Investigation, Writing - Original Draft, Project administration, Funding acquisition **Marcel Bliedtner:** Investigation, Writing - Review & Editing **Andrew S. Carr:** Investigation, Writing - Review & Editing **Julian Struck:** Investigation, Writing - Review & Editing **Nadia du Plessis:** Writing - Review & Editing **Bruno Glaser:** Methodology, Writing - Review & Editing **Michael E. Meadows:** Writing - Review & Editing **Lynne J. Quick:** Writing - Review & Editing **Michael Zech:** Methodology, Writing - Review & Editing **Roland Zech:** Conceptualization, Methodology, Writing - Review & Editing, Supervision, Project administration, Funding acquisition **Torsten Haberzettl:** Conceptualization, Methodology, Writing - Review & Editing, Supervision, Project administration, Funding acquisition.

Declaration of competing interest

The authors declare that they have no known competing financial interests or personal relationships that could have appeared to influence the work reported in this paper.

Acknowledgements

This study was funded by the German Research Foundation (DFG) (HA 5089/11–1; ZE 860/6–1). Sediment cores were recovered within the RAiN project. PS gratefully acknowledges the support by a fellowship from the state of Thuringia (Landesgraduiertenstipendium). Particularly acknowledged are Lucas Bittner, Nico Blaubach, Tobias Bromm, Christian David Gregori, Corinna Heinrich, Jana Löhrlein, Heike Maennicke, Carla May,

Mike Steinich, Magdalena Wagner and Marianne Zech for assistance in the lab.

Appendix A. Supplementary data

Supplementary data to this article can be found online at https://doi.org/10.1016/j.quascirev.2022.107467.

References

Amelung, W., Cheshire, M.V., Guggenberger, G., 1996. Determination of neutral and acidic sugars in soil by capillary gas-liquid chromatography after trifluoroacetic acid hydrolysis. Soil Biol. Biochem. 28, 1631–1639.

Bar-Matthews, M., Marean, C.W., Jacobs, Z., Karkanas, P., Fisher, E.C., Herries, A.I.R., Brown, K., Williams, H.M., Bernatchez, J., Ayalon, A., Nilssen, P.J., 2010. A high resolution and continuous isotopic speleothem record of paleoclimate and paleoenvironment from 90 to 53 ka from Pinnacle Point on the south coast of South Africa. Quat. Sci. Rev. 29, 2131–2145.

Bateman, M.D., Carr, A.S., Dunajko, A.C., Holmes, P.J., Roberts, D.L., McLaren, S.J., Bryant, R.G., Marker, M.E., Murray-Wallace, C.V., 2011. The evolution of coastal barrier systems: a case study of the Middle-Late Pleistocene Wilderness barriers, South Africa. Quat. Sci. Rev. 30, 63–81.

Blaauw, M., Christen, J.A., 2011. Flexible paleoclimate age-depth models using an autoregressive gamma process. Bayesian Anal. 6, 457–474.

Boom, A., Carr, A.S., Chase, B.M., Grimes, H.L., Meadows, M.E., 2014. Leaf wax n-alkanes and δ13C values of CAM plants from arid southwest Africa. Org. Geochem. 67, 99–102.

Bowen, G.J., 2020. The Online Isotopes in Precipitation Calculator. URL:, version 3.1. http://www.waterisotopes.org.

Bowen, G.J., Revenaugh, J., 2003. Interpolating the isotopic composition of modern meteoric precipitation. Water Resour. Res. 39, 1–10.

Bowen, G.J., Wassenaar, L.I., Hobson, K.A., 2005. Global application of stable hydrogen and oxygen isotopes to wildlife forensics. Oecologia 143, 337–348.

Braun, K., Bar-Matthews, M., Ayalon, A., Zilberman, T., Matthews, A., 2017. Rainfall isotopic variability at the intersection between winter and summer rainfall regimes in coastal South Africa (Mossel Bay, Western Cape Province). S. Afr. J. Geol. 120, 323–340.

Braun, K., Bar-Matthews, M., Matthews, A., Ayalon, A., Cowling, R.M., Karkanas, P., Fisher, E.C., Dyez, K., Zilberman, T., Marean, C.W., 2019. Late Pleistocene records of speleothem stable isotopic compositions from Pinnacle Point on the South African south coast. Quater. Res. 91, 265–288.

Braun, K., Bar-Matthews, M., Matthews, A., Ayalon, A., Zilberman, T., Cowling, R.M., Fisher, E.C., Herries, A.I.R., Brink, J.S., Marean, C.W., 2020. Comparison of climate and environment on the edge of the palaeo-Agulhas Plain to the Little karoo (South Africa) in marine isotope Stages 5–3 as indicated by speleothems. Quat. Sci. Rev. 235, 105803.

Breecker, D.O., 2017. Atmospheric pCO2 control on speleothem stable carbon isotope compositions. Earth Planet Sci. Lett. 458, 58–68.

Briant, R.M., Bateman, M.D., 2009. Luminescence dating indicates radiocarbon age underestimation in late Pleistocene fluvial deposits from eastern England. J. Quat. Sci. 24, 916–927.

Briant, R.M., Brock, F., Demarchi, B., Langford, H.E., Penkman, K.E.H., Schreve, D.C., Schwenninger, J.-L., Taylor, S., 2018. Improving chronological control for environmental sequences from the last glacial period. Quat. Geochronol. 43, 40–49.

British Oceanographic data centre (BODC), 2014. GEBCO's Gridded Bathymetric Data Sets (GEBCO_2014 Grid), 30 Arc Second Resolution. National Oceanographic Centre, Liverpool.

Carr, A.S., Boom, A., Dunajko, A., Bateman, M.D., Holmes, P.J., Berrio, J.-C., 2010. New evidence for the age and palaeoecology of the Knysna Formation, South Africa. S. Afr. J. Geol. 113, 241–256.

Carr, A.S., Chase, B.M., Boom, A., Meadows, M.E., Sanchez, J.M., 2022. Variability in soil and foliar stable carbon and nitrogen isotope compositions in the winter rainfall biomes of South Africa. J. Arid Environ. 200, 104726.

Cawthra, H.C., Bateman, M.D., Carr, A.S., Compton, J.S., Holmes, P.J., 2014. Understanding Late Quaternary change at the land–ocean interface: a synthesis of the evolution of the Wilderness coastline, South Africa. Quat. Sci. Rev. 99, 210–223.

Cawthra, H.C., Bergh, E.W., Wiles, E.A., Compton, J.S., 2021. Late Quaternary deep marine sediment records off southern Africa. S. Afr. J. Geol.

Cernusak, L.A., Wong, S.C., Farquhar, G.D., 2003. Oxygen isotope composition of phloem sap in relation to leaf water in Ricinus communis. Funct. Plant Biol. 30, 1059–1070.

Chase, B.M., Boom, A., Carr, A.S., Quick, L.J., Reimer, P.J., 2020. High-resolution record of Holocene climate change dynamics from southern Africa's temperate-tropical boundary, Baviaanskloof, South Africa. Palaeogeogr. Palaeoclimatol. Palaeoecol. 539, 109518.

Chase, B.M., Chevalier, M., Boom, A., Carr, A.S., 2017. The dynamic relationship between temperate and tropical circulation systems across South Africa since the last glacial maximum. Quat. Sci. Rev. 174, 54–62.

Chase, B.M., Meadows, M.E., 2007. Late Quaternary dynamics of southern Africa's winter rainfall zone. Earth Sci. Rev. 84, 103–138.

Chase, B.M., Quick, L.J., 2018. Influence of Agulhas forcing of Holocene climate change in South Africa's southern Cape. Quater. Res. 90, 303–309.

Cockcroft, M.J., Wilkinson, M.J., Tyson, P.D., 1987. The application of a present-day climatic model to the late quaternary in southern Africa. Climatic Change 10, 161–181.

Cohen, A.L., 1993. A Holocene Sea Surface Temperature Record in Mollusc Shells from the South African Coast, PhD Thesis. University of Cape Town, Cape Town.

Cohen, A.L., Tyson, P.D., 1995. Sea-surface temperature fluctuations during the Holocene off the south coast of Africa: implications for terrestrial climate and rainfall. Holocene 5, 304–312.

Colarossi, D., Duller, G.A.T., Roberts, H.M., Tooth, S., Botha, G.A., 2020. A comparison of multiple luminescence chronometers at Voordrag, South Africa. Quat. Geochronol. 60, 101094.

Croudace, I.W., Rindby, A., Rothwell, R.G., 2006. ITRAX: description and evaluation of a new multi-function X-ray core scanner. Geol. Soc. Lond. Sp. Publ. 267, 51–63.

Dansgaard, W., 1964. Stable isotopes in precipitation. Tellus 16, 436–468.

Diefendorf, A.F., Freimuth, E.J., 2017. Extracting the most from terrestrial plant-derived n-alkyl lipids and their carbon isotopes from the sedimentary record: a review. Org. Geochem. 103, 1–21.

du Plessis, N., Chase, B.M., Quick, L.J., Strobel, P., Haberzettl, T., Meadows, M.E., 2021. A c. 650 year pollen and microcharcoal record from Vankervelsvlei, South Africa. In: Runge, J., Gosling, W.D., Lézine, A.-M., Scott, L. (Eds.), Quaternary Vegetation Dynamics – the African Pollen Database. CRC Press, London, pp. 301–308.

DWD Climate Data Center, 2020. Recent and Historical Dataset: Monthly Mean Air Temperature for Station George Airport (CDC-ID 68828) worldwide, version recent, last accessed: 2020-07-01. https://opendata.dwd.de/climate_environment/CDC/observations_global/CLIMAT/.

Eglinton, T.I., Eglinton, G., 2008. Molecular proxies for paleoclimatology. Earth Planet Sci. Lett. 275, 1–16.

Engelbrecht, C.J., Landman, W.A., 2016. Interannual variability of seasonal rainfall over the Cape south coast of South Africa and synoptic type association. Clim. Dynam. 47, 295–313.

Engelbrecht, C.J., Landman, W.A., Engelbrecht, F.A., Malherbe, J., 2015. A synoptic decomposition of rainfall over the Cape south coast of South Africa. Clim. Dynam. 44, 2589–2607.

Engelbrecht, F.A., Marean, C.W., Cowling, R.M., Engelbrecht, C.J., Neumann, F.H., Scott, L., Nkoana, R., O'Neal, D., Fisher, E., Shook, E., Franklin, J., Thatcher, M., McGregor, J.L., Van der Merwe, J., Dedekind, Z., Difford, M., 2019. Downscaling last glacial maximum climate over southern Africa. Quat. Sci. Rev. 226, 105879.

ESRI Inc., 2020. World Imagery Online Basemap. Esri, DigitalGlobe, GeoEye, Earthstar Geographics, CNES/Airbus DS. USDA, USGS, Aerogrid, IGN, and the GIS User Community.

Farquhar, G.D., Ehleringer, J.R., Hubick, K.T., 1989. Carbon isotope discrimination and photosynthesis. Annu. Rev. Plant Physiol. Plant Mol. Biol. 40, 503–537.

Fick, S.E., Hijmans, R.J., 2017. WorldClim 2: new 1-km spatial resolution climate surfaces for global land areas. Int. J. Climatol. 37, 4302–4315.

Friedman, I., Redfield, A.C., Schoen, B., Harris, J., 1964. The variation of the deuterium content of natural waters in the hydrologic cycle. Rev. Geophys. 2, 177–224.

Gamarra, B., Sachse, D., Kahmen, A., 2016. Effects of leaf water evaporative 2H-enrichment and biosynthetic fractionation on leaf wax n-alkane δ2H values in C3 and C4 grasses. Plant Cell Environ. 39, 2390–2403.

Geldenhuys, C.J., 1988. Phytogeography of the southern Cape forest flora. FRD Occasion Rep. 45, 158–181.

Gessler, A., Brandes, E., Buchmann, N., Helle, G., Rennenberg, H., Barnard, R.L., 2009. Tracing carbon and oxygen isotope signals from newly assimilated sugars in the leaves to the tree-ring archive. Plant Cell Environ. 32, 780–795.

Haberzettl, T., Baade, J., Compton, J., Daut, G., Dupont, L., Finch, J., Frenzel, P., Green, A., Hahn, A., Hebbeln, D., Helmschrot, J., Humphries, M., Kasper, T., Kirsten, K., Mäusbacher, R., Meadows, M., Meschner, S., Quick, L., Schefuß, E., Wündsch, M., Zabel, M., 2014. Paleoenvironmental investigations using a combination of terrestrial and marine sediments from South Africa - The RAIN (Regional Archives for Integrated iNvestigations) approach. Zentralblatt für Geologie und Paläontologie, Teil I 2014, pp. 55–73.

Hahn, A., Schefuß, E., Andò, S., Cawthra, H.C., Frenzel, P., Kugel, M., Meschner, S., Mollenhauer, G., Zabel, M., 2017. Southern Hemisphere anticyclonic circulation drives oceanic and climatic conditions in late Holocene southernmost Africa. Clim. Past 13, 649–665.

Hahn, A., Schefuß, E., Groeneveld, J., Miller, C., Zabel, M., 2021. Glacial to interglacial climate variability in the southeastern African subtropics (25–20° S). Clim. Past 17, 345–360.

Hare, V.J., Loftus, E., Jeffrey, A., Ramsey, C.B., 2018. Atmospheric CO2 effect on stable carbon isotope composition of terrestrial fossil archives. Nat. Commun. 9, 252.

Harris, C., Burgers, C., Miller, J., Rawoot, F., 2010. O- and H-isotope record of Cape Town rainfall from 1996 to 2008, and its application to recharge studies of Table Mountain groundwater, South Africa. S. Afr. J. Geol. 113, 33–56.

Hepp, J., Mayr, C., Rozanski, K., Schäfer, I.K., Tuthorn, M., Glaser, B., Juchelka, D., Stichler, W., Zech, R., Zech, M., 2021. Validation of a coupled δ2Hn-alkane-δ18Osugar paleohygrometer approach based on a climate chamber experiment. Biogeosciences 18, 5363–5380.

Hepp, J., Schäfer, I.K., Lanny, V., Franke, J., Bliedtner, M., Rozanski, K., Glaser, B., Zech, M., Eglinton, T.I., Zech, R., 2020. Evaluation of bacterial glycerol dialkyl glycerol tetraether and 2H–18O biomarker proxies along a central European topsoil transect. Biogeosciences 17, 741–756.

Hepp, J., Tuthorn, M., Zech, R., Mügler, I., Schlütz, F., Zech, W., Zech, M., 2015.

Reconstructing lake evaporation history and the isotopic composition of precipitation by a coupled δ18O–δ2H biomarker approach. J. Hydrol. 529, 622–631.
Hepp, J., Wüthrich, L., Bromm, T., Bliedtner, M., Schäfer, I.K., Glaser, B., Rozanski, K., Sirocko, F., Zech, R., Zech, M., 2019. How dry was the younger dryas? Evidence from a coupled δ2H–δ18O biomarker paleohygrometer applied to the gemündener maar sediments, western eifel, Germany. Clim. Past 15, 713–733.
Hepp, J., Zech, R., Rozanski, K., Tuthorn, M., Glaser, B., Greule, M., Keppler, F., Huang, Y., Zech, W., Zech, M., 2017. Late Quaternary relative humidity changes from Mt. Kilimanjaro, based on a coupled 2H-18O biomarker paleohygrometer approach. Quat. Int. 438, 116–130. Part B.
Herrmann, N., Boom, A., Carr, A.S., Chase, B.M., West, A.G., Zabel, M., Schefuß, E., 2017. Hydrogen isotope fractionation of leaf wax n-alkanes in southern African soils. Org. Geochem. 109, 1–13.
Heyng, A.M., Mayr, C., Lücke, A., Wissel, H., Striewski, B., 2014. Late Holocene hydrologic changes in northern New Zealand inferred from stable isotope values of aquatic cellulose in sediments from Lake Pupuke. J. Paleolimnol. 51, 485–497.
Hogg, A.G., Heaton, T.J., Hua, Q., Palmer, J.G., Turney, C.S.M., Southon, J., Bayliss, A., Blackwell, P.G., Boswijk, G., Bronk Ramsey, C., Pearson, C., Petchey, F., Reimer, P., Reimer, R., Wacker, L., 2020. SHCal20 Southern Hemisphere calibration, 0–55,000 years cal BP. Radiocarbon 1–20.
Horita, J., Wesolowski, D.J., 1994. Liquid-vapor fractionation of oxygen and hydrogen isotopes of water from the freezing to the critical temperature. Geochem. Cosmochim. Acta 58, 3425–3437.
Hou, J., D'Andrea, W.J., MacDonald, D., Huang, Y., 2007. Evidence for water use efficiency as an important factor in determining the δD values of tree leaf waxes. Org. Geochem. 38, 1251–1255.
Howard-Williams, C., 1979. Distribution, biomass and role of aquatic macrophytes in Lake Sibaya. In: Allanson, B.R. (Ed.), Lake Sibaya,. Dr W Junk Publishers, Boston, pp. 88–107.
Huang, Y., Shuman, B., Wang, Y., Webb, T., Grimm, E.C., Jacobson, G.L., 2006. Climatic and environmental controls on the variation of C3 and C4 plant abundances in central Florida for the past 62,000 years. Palaeogeogr. Palaeoclimatol. Palaeoecol. 237, 428–435.
Illenberger, W.K., 1996. The geomorphologic evolution of the Wilderness dune cordons, South Africa. Quat. Int. 33, 11–20.
Irving, S.J.E., 1998. Late Quaternary Palaeoenvironments at Vankervelsvlei, Near Knysna, South Africa, Master Thesis. University of Cape Town, Rondebosch.
Irving, S.J.E., Meadows, M.E., 1997. Radiocarbon chronology and organic matter accumulation at Vankervelsvlei, near Knysna, South Africa. S. Afr. Geogr. J. 79, 101–105.
Johnson, M.R., Anhausser, C.R., Thomas, R.J., 2006. The Geology of South Africa. Geological Society of South Africa, Johannesburg/Council for Geoscience, Pretoria.
Lehmann, M.M., Gamarra, B., Kahmen, A., Siegwolf, R.T.W., Saurer, M., 2017. Oxygen isotope fractionations across individual leaf carbohydrates in grass and tree species. Plant Cell Environ. 40, 1658–1670.
Lemma, B., Bittner, L., Glaser, B., Kebede, S., Nemomissa, S., Zech, W., Zech, M., 2021. δ2Hn-alkane and δ18Osugar biomarker proxies from leaves and topsoils of the Bale Mountains, Ethiopia, and implications for paleoclimate reconstructions. Biogeochemistry 153, 135–153.
Lisiecki, L.E., Raymo, M.E., 2005. A Pliocene-Pleistocene stack of 57 globally distributed benthic δ18O records. Paleoceanography 20.
Liu, H., Liu, W., 2019. Hydrogen isotope fractionation variations of n-alkanes and fatty acids in algae and submerged plants from Tibetan Plateau lakes: implications for palaeoclimatic reconstruction. Sci. Total Environ. 695, 133925.
Mandiola, S.R., Grundling, A.T., Grundling, P.-L., van der Plicht, J., van der Waal, B.C.W., Grootjans, A.P., 2021. Ecohydrological analysis of a South African through-flow mire: Vankervelsvlei revisited. Mires Peat 27.
Merlivat, L., 1978. Molecular diffusivities of H2 16O, HD16O, and H2 18O in gases. J. Chem. Phys. 69, 2864–2871.
Miller, C., Hahn, A., Liebrand, D., Zabel, M., Schefuß, E., 2020. Mid- and low latitude effects on eastern South African rainfall over the Holocene. Quat. Sci. Rev. 229, 106088.
Mucina, L., Rutherford, M.C., 2006. The Vegetation of South Africa, Lesotho and Swaziland. SANBI, Pretoria.
NASA, J.P.L., 2013. NASA Shuttle Radar Topography Mission Global 1 Arc Second [Data Set]. NASA EOSDIS Land Processes DAAC. https://doi.org/10.5067/MEaSUREs/SRTM/SRTMGL1.003. Accessed 2020-12-29 from.
Neumann, F.H., Stager, J.C., Scott, L., Venter, H.J.T., Weyhenmeyer, C., 2008. Holocene vegetation and climate records from lake sibaya, KwaZulu-natal (South Africa). Rev. Palaeobot. Palynol. 152, 113–128.
Palstra, S.W.L., Wallinga, J., Viveen, W., Schoorl, J.M., van den Berg, M., van der Plicht, J., 2021. Cross-comparison of last glacial radiocarbon and OSL ages using periglacial fan deposits. Quat. Geochronol. 61, 101128.
Quick, L.J., Carr, A.S., Meadows, M.E., Boom, A., Bateman, M.D., Roberts, D.L., Reimer, P.J., Chase, B.M., 2015. A late Pleistocene–Holocene multi-proxy record of palaeoenvironmental change from Still Bay, southern Cape Coast, South Africa. J. Quat. Sci. 30, 870–885.
Quick, L.J., Chase, B.M., Wündsch, M., Kirsten, K., Chevalier, M., Mäusbacher, R., Meadows, M., Haberzettl, T., 2018. A high-resolution record of Holocene climate and vegetation dynamics from the southern Cape coast of South Africa: pollen and microcharcoal evidence from Eilandvlei. J. Quat. Sci. 1–14.
Quick, L.J., Meadows, M.E., Bateman, M.D., Kirsten, K.L., Mäusbacher, R., Haberzettl, T., Chase, B.M., 2016. Vegetation and climate dynamics during the last glacial period in the fynbos-afrotemperate forest ecotone, southern Cape, South Africa. Quat. Int. 404, 136–149. Part B.
Reinwarth, B., Franz, S., Baade, J., Haberzettl, T., Kasper, T., Daut, G., Helmschrot, J., Kirsten, K.L., Quick, L.J., Meadows, M.E., Mäusbacher, R., 2013. A 700-year record on the effects of climate and human impact on the southern Cape coast inferred from lake sediments of Eilandvlei, wilderness embayment, South Africa. Geografiska Annaler Ser. Phys. Geogr. 95, 345–360.
Sachse, D., Billault, I., Bowen, G.J., Chikaraishi, Y., Dawson, T.E., Feakins, S.J., Freeman, K.H., Magill, C.R., McInerney, F.A., van der Meer, M.T.J., Polissar, P., Robins, R.J., Sachs, J.P., Schmidt, H.L., Sessions, A.L., White, J.W.C., West, J.B., Kahmen, A., 2012. Molecular paleohydrology: interpreting the hydrogen- isotopic composition of lipid biomarkers from photosynthesizing organisms. Annu. Rev. Earth Planet Sci. 40, 221–249.
Schäfer, I.K., Bliedtner, M., Wolf, D., Kolb, T., Zech, J., Faust, D., Zech, R., 2018. A δ13C and δ2H leaf wax record from the Late Quaternary loess-paleosoil sequence El Paraíso, Central Spain. Palaeogeogr. Palaeoclimatol. Palaeoecol. 507, 52–59.
Schmidt, H.-L., Werner, R.A., Roßmann, A., 2001. 18O Pattern and biosynthesis of natural plant products. Phytochemistry 58, 9–32.
Schubert, B.A., Jahren, A.H., 2012. The effect of atmospheric CO2 concentration on carbon isotope fractionation in C3 land plants. Geochem. Cosmochim. Acta 96, 29–43.
Scott, L., Lee-Thorp, J.A., 2004. Holocene climatic trends and rhythms in southern Africa. In: Battarbee, R.W., Gasse, F., Stickley, C.E. (Eds.), Past Climate Variability through Europe and Africa. Springer, Dordrecht, pp. 69–91.
Sessions, A.L., 2016. Factors controlling the deuterium contents of sedimentary hydrocarbons. Org. Geochem. 96, 43–64.
Sessions, A.L., Burgoyne, T.W., Schimmelmann, A., Hayes, J.M., 1999. Fractionation of hydrogen isotopes in lipid biosynthesis. Org. Geochem. 30, 1193–1200.
Shi, F., Rao, Z., Cao, J., Huang, C., Wu, D., Yang, W., Sun, W., 2019a. Meltwater is the dominant water source controlling α-cellulose δ18O in a vascular-plant-dominated alpine peatland in the Altai Mountains, Central Asia. J. Hydrol. 572, 192–205.
Shi, F., Rao, Z., Li, Y., Cao, J., Shi, X., Li, C., Sun, W., 2019b. Precipitation δ18O recorded by the α-cellulose δ18O of plant residues in surface soils: evidence from a broad environmental gradient in inland China. Global Biogeochem. Cycles 33, 1440–1468.
Singarayer, J.S., Burrough, S.L., 2015. Interhemispheric dynamics of the African rainbelt during the late Quaternary. Quat. Sci. Rev. 124, 48–67.
Sternberg, d.L., 1989. Oxygen and hydrogen isotope ratios in plant cellulose: mechanisms and applications. In: Rundel, P.W., Ehleringer, J.R., Nagy, K.A. (Eds.), Stable Isotopes in Ecological Research. Springer New York, New York, NY, pp. 124–141.
Sternberg, L., DeNiro, M.J., 1983. Isotopic composition of cellulose from C3, C4 and CAM plants growing near one another. Science 220, 947–949.
Sternberg, L., Deniro, M.J., Savidge, R.A., 1986. Oxygen isotope exchange between metabolites and water during biochemical reactions leading to cellulose synthesis. Plant Physiol. 82, 423–427.
Strobel, P., Bliedtner, M., Carr, A.S., Frenzel, P., Klaes, B., Salazar, G., Struck, J., Szidat, S., Zech, R., Haberzettl, T., 2021. Holocene sea level and environmental change at the southern Cape - an 8.5 kyr multi-proxy paleoclimate record from lake Voëlvlei, South Africa. Clim. Past 17, 1567–1586.
Strobel, P., Haberzettl, T., Bliedtner, M., Struck, J., Glaser, B., Zech, M., Zech, R., 2020. The potential of δ2Hn-alkanes and δ18Osugar for paleoclimate reconstruction – a regional calibration study for South Africa. Sci. Total Environ. 716, 137045.
Strobel, P., Kasper, T., Frenzel, P., Schittek, K., Quick, L.J., Meadows, M.E., Mäusbacher, R., Haberzettl, T., 2019. Late Quaternary palaeoenvironmental change in the year-round rainfall zone of South Africa derived from peat sediments from Vankervelsvlei. Quat. Sci. Rev. 218, 200–214.
Struck, J., Bliedtner, M., Strobel, P., Bittner, L., Bazarradnaa, E., Andreeva, D., Zech, W., Glaser, B., Zech, M., Zech, R., 2020. Leaf waxes and hemicelluloses in topsoils reflect the δ2H and δ18O isotopic composition of precipitation in Mongolia. Front. Earth Sci. 8.
Stuiver, M., Reimer, P.J., Reimer, R.W., 2020. CALIB 8.2 [WWW program] at. http://calib.org. (Accessed 20 August 2020).
Talma, A.S., Vogel, J.C., 1992. Late quaternary paleotemperatures derived from a speleothem from Cango caves, Cape province, South Africa. Quater. Res. 37, 203–213.
Trabucco, A., Zomer, R., 2019. Global aridity Index and potential evapotranspiration (ET0) climate database v2. figshare. Fileset.
Tuthorn, M., Zech, M., Ruppenthal, M., Oelmann, Y., Kahmen, A., Valle, H.F.d., Wilcke, W., Glaser, B., 2014. Oxygen isotope ratios (18O/16O) of hemicellulose-derived sugar biomarkers in plants, soils and sediments as paleoclimate proxy II: insight from a climate transect study. Geochem. Cosmochim. Acta 126, 624–634.
Tuthorn, M., Zech, R., Ruppenthal, M., Oelmann, Y., Kahmen, A., del Valle, H.F., Eglinton, T., Rozanski, K., Zech, M., 2015. Coupling δ2H and δ18O biomarker results yields information on relative humidity and isotopic composition of precipitation - a climate transect validation study. Biogeosciences 12, 3913–3924.
Tyson, P.D., Preston-Whyte, R.A., 2000. The Weather and Climate of Southern Africa. Oxford University Press, Cape Town.
van Zinderen Bakker, E.M., 1976. The evolution of late Quaternary paleoclimates of Southern Africa. Palaeoecol. Afr. 9 9, 160–202.
Voelker, S.L., Brooks, J.R., Meinzer, F.C., Anderson, R., Bader, M.K.-F., Battipaglia, G., Becklin, K.M., Beerling, D., Bert, D., Betancourt, J.L., Dawson, T.E., Domec, J.-C., Guyette, R.P., Körner, C., Leavitt, S.W., Linder, S., Marshall, J.D., Mildner, M.,

Ogée, J., Panyushkina, I., Plumpton, H.J., Pregitzer, K.S., Saurer, M., Smith, A.R., Siegwolf, R.T.W., Stambaugh, M.C., Talhelm, A.F., Tardif, J.C., Van de Water, P.K., Ward, J.K., Wingate, L., 2016. A dynamic leaf gas-exchange strategy is conserved in woody plants under changing ambient CO2: evidence from carbon isotope discrimination in paleo and CO2 enrichment studies. Global Change Biol. 22, 889–902.

Voelker, S.L., Brooks, J.R., Meinzer, F.C., Roden, J., Pazdur, A., Pawelczyk, S., Hartsough, P., Snyder, K., Plavcová, L., Šantrůček, J., 2014. Reconstructing relative humidity from plant δ18O and δD as deuterium deviations from the global meteoric water line. Ecol. Appl. 24, 960–975.

Voelker, S.L., Stambaugh, M.C., Guyette, R.P., Feng, X., Grimley, D.A., Leavitt, S.W., Panyushkina, I., Grimm, E.C., Marsicek, J.P., Shuman, B., Brandon Curry, B., 2015. Deglacial hydroclimate of midcontinental north America. Quater. Res. 83, 336–344.

Waelbroeck, C., Labeyrie, L., Michel, E., Duplessy, J.C., McManus, J.F., Lambeck, K., Balbon, E., Labracherie, M., 2002. Sea-level and deep water temperature changes derived from benthic foraminifera isotopic records. Quat. Sci. Rev. 21, 295–305.

Weldon, D., Reason, C.J.C., 2014. Variability of rainfall characteristics over the South Coast region of South Africa. Theor. Appl. Climatol. 115, 177–185.

Wirth, S.B., Sessions, A.L., 2016. Plant-wax D/H ratios in the southern European Alps record multiple aspects of climate variability. Quat. Sci. Rev. 148, 176–191.

Wissel, H., Mayr, C., Lücke, A., 2008. A new approach for the isolation of cellulose from aquatic plant tissue and freshwater sediments for stable isotope analysis. Org. Geochem. 39, 1545–1561.

Wündsch, M., Haberzettl, T., Cawthra, H.C., Kirsten, K.L., Quick, L.J., Zabel, M., Frenzel, P., Hahn, A., Baade, J., Daut, G., Kasper, T., Meadows, M.E., Mäusbacher, R., 2018. Holocene environmental change along the southern Cape coast of South Africa – insights from the Eilandvlei sediment record spanning the last 8.9 kyr. Global Planet. Change 163, 51–66.

Wündsch, M., Haberzettl, T., Kirsten, K.L., Kasper, T., Zabel, M., Dietze, E., Baade, J., Daut, G., Meschner, S., Meadows, M.E., Mäusbacher, R., 2016. Sea level and climate change at the southern Cape coast, South Africa, during the past 4.2 kyr. Palaeogeogr. Palaeoclimatol. Palaeoecol. 446, 295–307.

Yakir, D., DeNiro, M.J., 1990. Oxygen and hydrogen isotope fractionation during cellulose metabolism in lemna gibba L. Plant Physiol. 93, 325–332.

Zech, M., Glaser, B., 2009. Compound-specific δ18O analyses of neutral sugars in soils using gas chromatography–pyrolysis–isotope ratio mass spectrometry: problems, possible solutions and a first application. Rapid Commun. Mass Spectrom. 23, 3522–3532.

Zech, M., Mayr, C., Tuthorn, M., Leiber-Sauheitl, K., Glaser, B., 2014. Oxygen isotope ratios (18O/16O) of hemicellulose-derived sugar biomarkers in plants, soils and sediments as paleoclimate proxy I: insight from a climate chamber experiment. Geochem. Cosmochim. Acta 126, 614–623.

Zech, M., Tuthorn, M., Detsch, F., Rozanski, K., Zech, R., Zöller, L., Zech, W., Glaser, B., 2013. A 220ka terrestrial δ18O and deuterium excess biomarker record from an eolian permafrost paleosol sequence, NE-Siberia. Chem. Geol. 360–361, 220–230.

Zech, M., Werner, R.A., Juchelka, D., Kalbitz, K., Buggle, B., Glaser, B., 2012. Absence of oxygen isotope fractionation/exchange of (hemi-) cellulose derived sugars during litter decomposition. Org. Geochem. 42, 1470–1475.

Zech, M., Zech, R., Rozanski, K., Gleixner, G., Zech, W., 2015. Do n-alkane biomarkers in soils/sediments reflect the δ2H isotopic composition of precipitation? A case study from Mt. Kilimanjaro and implications for paleoaltimetry and paleoclimate research. Isot. Environ. Health Stud. 51, 508–524.

Zhao, X., Dupont, L., Schefuß, E., Meadows, M.E., Hahn, A., Wefer, G., 2016. Holocene vegetation and climate variability in the winter and summer rainfall zones of South Africa. Holocene 26, 843–857.